Spatial and temporal variations in slip rate over millions of years on an extensional fault system and implications for seismic hazard

Billy. J. Andrews[1], Zoë. K. Mildon[1], Christopher A-L. Jackson[2,3], Constanza Rodriguez Piceda[1], Francesco Iezzi[4], Gerald P. Roberts[5] and Joanna P. Faure Walker[6]

[1]School of Geography, Earth and Environmental Sciences, University of Plymouth, Drake Circus, Plymouth, PL4 8AA, UK

[2]Department of Earth Science & Engineering, Imperial College, Prince Consort Road, London, SW7 2BP, UK

[3]WSP UK Ltd, 8 First Street, Manchester, M14 4RP, UK

[4]Department of Earth Sciences, Environment and Resources, University of Naples Federico II, Naples, Italy

[5]School of Natural Sciences, Birkbeck, University of London, Malet Street, London, WC1E 7HX, UK

[6]Department of Risk and Disaster Reduction, University College London, Gower Street, London, WC1E 6BT, UK

Corresponding author: Billy Andrews (billy.andrews@plymouth.ac.uk)

Key Points:

- Slip rates on normal faults vary by up to 2 orders of magnitude over a few million years
- Within a fault network, the slip rates and the shape of slip rate profiles on individual faults are variable during different time periods
- In a network of faults, the recurrence interval for M>5 earthquakes can remain constant with the contribution from individual faults varying

Abstract

Slip rate is a key input for fault-based seismic hazard assessment, with temporal and spatial variations in slip rate along and between faults influencing earthquake size and recurrence. Temporal variations in slip rate have been attributed to earthquake clustering and anti-clustering in tectonically active settings. Here we explore the combined temporal and spatial assessment of slip rate variations of individual faults and the network they form part of. We present slip rates derived from a seismically imaged, presently-inactive fault network, from offshore NW Australia. This region underwent extension from the Upper Triassic (209.5 Ma) to Early Cretaceous (137.3 Ma) related to continental breakup, and it represents a low strain region as the maximum slip rates are <0.1 mm/yr. We show spatial and temporal slip rate variations across million-year time scales for individual faults within a network of across-strike faults. Slip rate profiles also differed through time, with the location of maximum slip rate on individual faults migrating along-strike by several kilometres between time periods (over 10^6 to 10^7 million years). We then calculate the resulting temporal variations in earthquake occurrence arising from the changes in slip rates. We show that within a fault network, whilst overall the earthquake recurrence rates over the entire fault system remain similar, recurrence rates on individual faults vary on the million-year timescales we study. Spatial and temporal variability of slip rate can introduce uncertainty in earthquake probability calculations, highlighting the need to incorporate this into probabilistic seismic hazard assessments.

Plain Language Summary

Understanding a faults slip rate is essential for assessing seismic hazard. Slip rates are not always constant, but can speed up or slow down. Additionally, where faults occur within a network, the proportion of slip accommodated by a particular fault can vary. These changes affect how often earthquakes occur and how hazard is distributed across a region.

In this study, we use 3D seismic data to examine an ancient fault network preserved offshore NW Austrailia. Although these faults are no longer active, they record millions of years of slip, allowing us to study how slip rates changes through time and across the network. We found that both the speed and location of slip on individual faults varied, with the areas of maximum slip rate shifting by kilometers along a given fault between time periods.

While the overall activity of the fault network remained broadly consistent through much of its history, individual faults showed large changes in slip rate. During the final time period, the entire network accelerated by a factor of ten. These variations directly affected calculated earthquake recurrence rates and therefore highlight how seismic hazard can shift through time across a fault network.

1 Introduction

Slip rates are an important input into fault-based probabilistic seismic hazard assessment (PSHA) (Chartier et al., 2019; Faure Walker et al., 2019; Pace et al., 2016; Youngs & Coppersmith, 1985), as they influence the moment accumulation rate and, therefore, the earthquake occurrence rates (Brune, 1968). Fault-based PSHA relies on the available data describing the fault activity, and these are often restricted to one single measurement of slip-rate on a fault, that is calculated for a specific period of time (e.g., Gómez-Novell et al., 2020; Valentini et al., 2017; Williams et al., 2023) However, slip-rates on both active and inactive faults are known to vary over decadal to million year timescales (Friedrich et al., 2003; Roberts et al., 2024). Most previous studies into temporal slip-rate variability have focused on a single along-strike location on a fault, for example paleoseismic trenching studies (e.g. Dolan et al., 2016; Nicol et al., 2010; Onderdonk et al., 2015; Wechsler et al., 2018; Zinke et al., 2019) or cosmogenic isotope studies (Goodall et al., 2021; Mechernich et al., 2018), although some studies do integrate numerous single locations across a region to discuss the broader behaviour of the fault network (Cowie et al., 2017; Dolan et al., 2007; Iezzi et al., 2021; Mildon et al., 2022; Nicol et al., 2010; Roberts et al., 2024; Sgambato et al., 2025). For normal faults, maximum displacement (and thus slip rate) is commonly observed near the centre of the fault, and displacement (or throw) profile are commonly assumed to show a broadly bell-shaped, elliptical or triangular form (Cowie & Scholz, 1992; Manighetti et al., 2004; Manzocchi et al., 2006; Nicol et al., 2005; Roberts, 2007). However, slip rates and total displacement show further variability along-strike (Cartwright & Mansfield, 1998; Faure Walker et al., 2009, 2010, 2012, 2019; Iezzi et al., 2020; McClymont et al., 2009; Roberts & Michetti, 2004; Sgambato et al., 2020).

The effect of spatial-temporal variations in slip-rate of the kind described above on PSHA remains relatively understudied (Faure Walker et al., 2019; Pace et al., 2014; Roberts et al., 2024; Scotti et al., 2021). Faure Walker et al. (2019) investigated how along-strike changes in slip-rate on a single fault affect the resulting seismic hazard. They found that different shapes of slip-rate profiles affect the resulting seismic hazard curves, with probability calculations varying for different profiles shapes beyond the uncertainty of Ground Motion Prediction Equations. This highlights the importance of collecting high-spatial resolution slip rate data. However, as slip-rate can also vary temporally, the magnitude and the position of maximum slip along an individual fault may also vary through time (Benedetti et al., 2002, 2013; Cowie et al., 2017; Iezzi et al., 2021; Roberts et al., 2024, 2025), and thus the location of maximum slip within a fault network may also vary. Understanding how throw accumulates through time, and therefore how slip-rate evolves, is an important consideration for seismic hazard assessments (Figure 1a). By investigating how much natural variability in slip-rate evolution might be

expected, this can be incorporated as a source of uncertainty in fault-based PSHA (e.g. Cowie et al., 2017; Roberts et al., 2025).

Faults do not occur in isolation but instead form networks of relatively closely spaced structures (e.g., Duffy et al., 2017; Morley and Nixon, 2016; Nicol et al., 2020; Nixon et al., 2014b; 2024). It is well-established that faults within broader networks interact over a range of temporal (decadal to million years) and spatial (10s m to >100 km) scales, directly controlling their slip rate and the related earthquake parameters (e.g., recurrence and magnitude). Mechanisms of fault interaction are not mutually exclusive and may include a combination of co- and interseismic stress changes (Gupta & Scholz, 2000; Harris & Simpson, 1998; Stein, 1999), the stress interaction between lower-crustal shear zones to which upper-crustal faults are geometrically and kinematically connected (Mildon et al., 2022; Roberts et al., 2024), and strain localisation as a fault network evolves (Cowie et al., 2005; Nicol et al., 1997; Nixon et al., 2024). Short-timescale fault interaction has in places been considered within seismic hazard studies, either via Coulomb stress changes (Pace et al., 2014; Toda & Enescu, 2011; Toda & Stein, 2018; Verdecchia et al., 2019) or by testing different fault segmentation scenarios and their potential to produce multiple fault ruptures (Mignan et al., 2015; Milner et al., 2013). Over longer time scales (i.e., > Myrs), while it is well-established that faults interact, affecting their throw accumulation (e.g., Childs et al., 2019; Fossen & Rotevatn, 2016; Nixon et al., 2024; Pan et al., 2022), it is unclear how fault interactions will affect calculated earthquake rates across the network, contributing to the regional earthquake occurrence, compared to earthquake rates on individual faults) (Figure 1b).

3D seismic reflection surveys can be used to investigate slip rate variability over long timescales (>Myr). Stratigraphic successions imaged and used to infer slip-rate patterns are often deposited over tens of millions of years, far longer than timescales typically resolved for presently active faults, enabling long-term variations in slip rate to be explored. Several assumptions and limitations must be considered when using 3D seismic data including subjective bias of the interpreter (Andrews et al., 2024; Bond, 2015), the need for sedimentation rates to exceed throw rates (Childs et al., 2003; Jackson et al., 2017), uncertainties and resolution of age data relating to mapped reflectors (e.g., Reeve et al., 2016), and the need of a reliable velocity model to convert throw and fault dip from time to meters (Holden et al., 2024) which can also introduce uncertainties in the interpreted fault dip. Despite these caveats, 3D seismic reflection dataset image the full three-dimensional geometry of faults, allowing us to explore spatial patterns in slip-rate with a dense sample spacing (100 m), and at multiple structural levels. Additionally, slip-rate profiles can be used to infer how fault length, and therefore the maximum expected earthquake magnitude, evolved through time (Meyer et al., 2002; Nicol et al., 2020; Walsh et al., 2002). Such measurements are often not possible on active faults, where the along-strike exposure of the fault is limited to the present-

134 day surface, may not be continuous, and/or the geomorphology may not be appropriate to
135 extract slip-rate values.

136 In this study, we address two key questions related to the slip rate variability in a normal
137 fault network. The first question is: how does displacement accumulate along a fault over time?
138 We test two hypotheses: (1) the position of maximum slip remains fixed over time, or (2) it
139 varies temporally. To address these hypotheses, we construct fault slip histories across a
140 kinematically linked normal fault network over four to eight time periods spanning 72.2 million
141 years. This analysis is based on a 3D seismic reflection survey from offshore NW Australia, a
142 region that experienced Jurassic and Cretaceous rifting, which resulted in the formation of an
143 extensive normal fault network. We interpret several age-constrained seismic horizons, dated
144 using wells within the study area, and use horizon offsets and ages to infer slip rates along
145 selected faults. We first document the spatial and temporal variability of slip rates along a
146 single, geometrically isolated fault, before expanding to consider the broader fault network.
147 The second question we address is how does displacement accumulate across a fault network
148 over time? (Figure 1b). We test two hypotheses: (1) the proportion of displacement taken up by
149 individual faults is constant over time, or (2) the proportion of displacement taken up by
150 individual faults varies. Finally, we use the derived slip rates to infer how the average annual
151 earthquake occurrence rate would have changed through time and discuss the implications of
152 our findings for seismic hazard assessment.

153 **2 Geological setting**

154 This study focuses on a fault network situated in the Exmouth Plateau region of the
155 Northern Carnarvon Basin, offshore NW Australia (Fig 2a, b). The ~400 km wide Exmouth
156 Plateau lies outboard of several sub-basins (Fig 2a) and is characterised by a complex
157 tectonostratigraphic history (Bilal & McClay, 2022; Gartrell et al., 2016; Gartrell, 2000). The
158 area experienced three main phases of extension: 1) NW-SE directed extension during the Late
159 Carboniferous to Permian that imparted a structural grain across much of the Northern
160 Carnarvon Basin (Bilal & McClay, 2022; Deng & McClay, 2019, 2021; Etheridge & O'Brien, 1994;
161 Gartrell, 2000), 2) Lower to Middle Triassic extension evident across west-dipping NE-SW to
162 NNW-SSW normal faults (Bilal & McClay, 2022), and 3) Upper Triassic to Middle Jurassic (209.5
163 to 162.5 Ma) ~E-W directed extension that caused wedge-shaped growth strata to develop
164 along N-S to NNE-SSW trending faults (Bilal et al., 2020; Bilal & McClay, 2022; Black et al., 2017;
165 Karner & Driscoll, 1999; Lathrop et al., 2021) (Fig. 2c), with this being the phase of extension
166 that we focus on. Between the Lower to Middle Triassic extension, and initiation of Upper
167 Triassic extension, a ~400 m thick succession of fluvio-deltaic sandstones and mudstones of the
168 Mungaroo formation blanketed the earlier phase of extension. Following the main phases of
169 extension (162.5 to 137.3 Ma), minor throw accumulation continued through local fault

reactivation and tip propagation in an otherwise post-rift phase (Black et al., 2017; Direen et al., 2008). Igneous activity throughout the Late Jurassic to Early Cretaceous resulted in widespread sill and dyke emplacement across the Exmouth Plateau (Direen et al., 2008; Magee and Jackson, 2020, 2021). Dyke emplacement is associated with dyke-induced faults that form narrow grabens, striking parallel to underlying dykes and extending to from the paleo-seabed to the upper dyke tip (Fig 2c) (e.g., Magee and Jackson, 2020, 2021; Magee et al., 2023). These faults typically exhibit displacements < 20 m (Magee and Jackson, 2021; Magee et al., 2023), whereas the studied faults have displacements of hundreds of metres. We do not find any dyke induced faults that cross-cut the studied fault network (Fig. 2c), with only the potential of minor interaction with Fault 1, and the studied fault network does not show the characteristic dyke-induced narrow grabens. Therefore, we suggest that dyke-related reactivation will be negligible and not impact the overall conclusions drawn in this study. Following dyke emplacement, deposition was dominated by passive margin sequences (137.3 to 0 Ma) following continental breakup during a period of thermal subsidence and passive margin development (Black et al., 2017; Direen et al., 2008).

In this study, we explore slip-rate evolution from the Upper Triassic (209.5 Ma) through to the end of the post-rift phase (137.3 Ma). The Exmouth Plateau was starved of sediment input throughout active rifting (Reeve et al., 2016, 2022). This caused large offset faults to have a surface expression at the time of faulting and undergo footwall degradation, and most faults to have condensed footwall stratigraphic successions (Bilal & McClay, 2022; Karner & Driscoll, 1999). The faults in our study area show no evidence of footwall degradation and most horizons are preserved on both the footwall and hanging wall of all faults, suggesting subsidence rate exceeded sediment accumulation rate for the studied fault network. Following the main phase of extension, some major faults in the Exmouth Plateau underwent 'tip-retreat', whereby fault length decreases with continued throw accumulation becomes localised towards the centre of the fault (Lathrop et al., 2022). The long-lived nature of the studied faults and lack of footwall degradation enable us to explore how slip rate differs through space and time across a complex fault network over >70 Myr.

3 Methods

3.1 Seismic reflection interpretation and data extraction

3.1.1 Seismic reflection data

The fault network in this study is imaged in the Chandon3D seismic cube (Fig 2), a 3D, time-migrated, zero-phase seismic reflection survey that has a record length of 6 s two-way-time (TWT) and a bin spacing of 25 m. Seismic data is displayed in SEG reverse polarity, where a downward increase in acoustic impedance corresponds to a trough (black) reflection, and a

downward decrease in acoustic impedance corresponds to a peak (red) reflection. The spatial resolution within the interval of interest (2.9 to 3.4 s TWT) is estimated by calculating the limits of separability (the minimum vertical distance whereby interfaces will produce distinct reflectors, ~17-21 m) and visibility (the vertical distance where interfaces are indistinguishable from background noise, 2-3 m) (Brown, 2011).

3.1.2 Borehole data and age framework

To constrain the age and lithology of mapped reflectors, we tied four different boreholes (Chandon-1, Chandon-2, Chandon-3 and Yellowglen, located 25.5 km west of Chandon-1) to the survey, with well reports available through the Geoscience Australia Portal (https://portal.ga.gov.au/). Boreholes were drilled into the footwalls of tilted blocks and extend into the upper portion of the Mungaroo Formation. They contain information about the depth and age of formation tops, alongside geophysical information such as gamma ray, sonic, neutron porosity, and bulk density data. We use age data derived from biostratigraphic information reported in the well reports to constrain the age of five reflectors between the Top Mungaroo (209.5 Ma) and the Top Upper Barrow (137.3 Ma) Formations. Due to stratigraphic thinning of the footwall, some regional reflectors are not observed in the boreholes (e.g., subdivisions of the Athol Formation). To account for this, and to expand our age framework we inferred the age of an additional four reflectors assuming constant sedimentation rates between age constrained reflectors (after Lathrop et al., 2021; Pan et al., 2022).

3.1.3 Seismic interpretation and calculation of slip rate

Slip rate can be calculated for faults where subsidence rate exceeds throw rate and the age of mapped horizons are known (e.g., due to well ties) (e.g., Childs et al., 2003; Lathrop et al., 2021; Nicol et al., 2005; Pan et al., 2022). In this study we interpret nine age constrained reflectors that could be mapped across the studied fault network to investigate slip-rate variations across eight time periods (Fig 2d). To construct throw profiles on each mapped horizon we use a series of transects spaced at 100 m and perpendicular to the fault trace (e.g. Fig. 2c). At each sample location, we collect fault cut-off data that includes near-fault continuous deformation for each horizon by projecting the regional dip of the horizon onto the fault plane and measuring the projected footwall and hanging wall horizon-fault plane cut-off pairs (Figure S1). Continuous deformation will account for the long-term strain accumulated on the fault and includes non-discrete strain (e.g., folding) and/or brittle deformation that is below the limit of separability of the dataset (e.g., Childs et al., 2017; Delogkos et al., 2020).

Cut-off pairs are converted from TWT to meters by using a velocity model constructed by fitting a polynomial best fit to the combined check-shot data from the nearby wells

(Supplementary 1) and used to calculate throw for each horizon. To calculate slip-rate across two horizons (H1 and H2), the difference in throw is calculated as:

$$\Delta throw = throw_{H2} - throw_{H1} \quad \text{(Equation 1)}$$

For cases where Δthrow is positive, indicating accumulated slip across the horizons, we used the dip across H2 to convert Δthrow to the change in slip:

$$slip\ (m) = \frac{\Delta throw}{\sin(dip_{H2})} \quad \text{(Equation 2)}$$

Equation 2 assumes that displacement across the fault is purely dip-slip (i.e., the slip vector is perpendicular to the measurement transect), and that the present-day dip of the fault can be considered representative of fault dip at the time of extension. If Δthrow is <0, indicating no slip accumulation, slip-rate will be zero at this location. We then used Δslip to calculate the slip-rate by dividing by the difference in age between H1 and H2 (Equation 3):

$$Slip\ rate\ \left(\frac{mm}{yr}\right) = \frac{\Delta Slip_{H2H1} \cdot 1000}{Age_{H2} - Age_{H1}} \quad \text{(Equation 3)}$$

We repeated these calculations at each paired cut-off, as well as for the deepest and shallowest mapped horizons, to calculate the time-averaged slip rate (i.e., 209.5 to 137.3 Mya). For the latter, we used a rift-average dip (dip_{RA}) to convert Δthrow to Δslip by considering the difference in depth and horizontal distance between the footwall pick across H1 and the hanging wall pick across TM.

3.1.4 Uncertainty in our slip rate calculations

Age of mapped horizons: Uncertainty in horizon age may arise from errors in formation ties or from uncertainties and/or the vertical spacing of biostratigraphic data used to derive formation ages from well data. This is the case for the Mesozoic succession, where published ages differ across the Exmouth Plateau. For instance, the Top Mungaroo (TM) has an age of 209.5 Ma within the sample area, whereas elsewhere in the Exmouth Plateau it ranges from 210 to 204 Ma (Reeve et al., 2022). In this study, we take ages from local well reports as we are interested in relative changes in slip-rate across a fault network and not across the basin. Additional uncertainty in age occurs where we have inferred age based on constant sedimentation rates. If this assumption does not hold, then the absolute slip-rate between time periods bounded by these reflectors may be either overestimated or underestimated relative to the true value. However, as the same age is used throughout the study area, these horizons with inferred ages act as 'time-lines', and the shape of slip-rate profiles as well as relative slip-

rate between faults within that time period will be unaffected by this uncertainty providing a greater temporal resolution of slip rate variations across the network.

To account for uncertainty in absolute horizon age, we apply a uniform ±0.25 Myr error to horizon ages when calculating minimum and maximum slip-rate values. Given that most ages are reported to 0.1 Myr precision, this represents a conservative estimate that is sufficient to encompass regional uncertainties and inferred horizon ages. Additionally, because the slip rates are calculated over time periods much longer than these uncertainties, applying ±0.25 Myr provides an appropriate propagation of age uncertainty through the slip-rate calculations while still relying on the local well-derived ages as reliable references.

Horizon mapping and correlation across faults: Horizon picks rely on consistent waveform reflections (Brown, 2011), and as this study requires information about the age of the reflector, horizons should ideally be linked to well data (Schaaf & Bond, 2019). To mitigate uncertainties and ensure consistency across the study area, we selected a fault network near three wells (Fig 2b), allowing horizons to be mapped confidently around fault tips (Bond, 2015; Chellingsworth et al., 2015). Whilst the significant footwall degradation observed elsewhere in the Exmouth Plateau (Barrett et al., 2021; Bilal et al., 2020; Martinez et al., 2024) was not present in the study area, footwall stratigraphy was sometimes condensed, locally hindering the mapping of horizons. Where a horizon is only missing in the footwall, we take the cut-off of the next youngest horizon as the footwall cutoff, thereby constraining the minimum throw across this specific horizon. Where the horizon is missing on both sides of the fault, slip rate is calculated for this sample point using the Δthrow to the next youngest horizon (i.e., if H2 was missing, slip rate would be calculated between H3 and H1). This method ensures that there are no gaps in the slip-history and does not significantly impact the shape or magnitude of the resultant slip rate profile.

Fault interpretation: Uncertainties in fault interpretation stem from an interpreter's conceptual model of the study area, seismic reflection strength, image quality and vertical exaggeration (Alcalde et al., 2017; Schaaf & Bond, 2019). To limit any differences across the study area, we maintained a constant vertical exaggeration (~1:3), and as the reflectors are well-imaged in the interval of interest and our interpretations conform to the region's tectonics (Fig 2c), anticipate minimal and consistent uncertainty in interpreting the position of faults.

Cut-off extraction: The interpretation of how reflections intersect faults (i.e., cut-offs) involves uncertainty influenced by the type of measured cut-off (discontinuous or continuous), the obliquity of the measurement transects, and the positioning of the horizon and fault (Andrews et al., 2024; Faleide et al., 2021; Magee et al., 2023). These uncertainties affect the extraction of key fault parameters used in our slip-rate calculations (e.g., throw, dip). To

mitigate against obliquity errors, all cut-off pairs are picked on a transect with a measurement obliquity of <15˚ (Andrews et al., 2024). Throw values that take into account continuous deformation introduce more uncertainty that those that do not due to the interpreter having to extrapolate regional dip onto the fault plane (Andrews et al., 2024). However, because the initial stage of fault growth across the Exmouth Plateau includes localised monocline development (Pan et al., 2022), continuous deformation needs to be considered in in our investigation of long-term slip-rate. To account for uncertainties in throw and dip, we applied error values of the greater value of ±8% or ±3 m for throw and ±14% or ±5˚ for dip, consistent with values reported by Andrews et al. (2024) from the same seismic cube.

Depth conversion: The method used for depth-conversion can influence the extracted fault parameters (Holden et al., 2024). In our study, we employed a polynomial fit to check-shot data. Given that the depth of the studied faults is similar and throw across faults modest (<456 m), any errors arising from the depth conversion are internally consistent in the study and are thus not considered with the throw errors used to calculate slip-rate.

Compaction-related loss of throw: The studied faults are deeply buried (i.e., 2 to 3 km), meaning compaction could rotate faults to less than their syn-extensional dip (Allen & Allen, 2013), thereby reducing throw across syn-sedimentary faults by <15% (Taylor et al., 2008). In this study, we do not undertake decompaction due to the similar depth of the faults, relatively uniform lithologies (Bilal & McClay, 2022), and uncertainties in decompaction parameters, particularly for the hanging wall sediments that are not penetrated by wells. Consequently, our slip-rate estimates represent a minimum, noting post-slip compaction, whilst affecting absolute values, is thought to have a negligible effect on the overall patterns of slip-rate across the fault network (Taylor et al., 2008).

To account for uncertainties in slip rate (SR) estimates, we calculate the minimum (SR_{min}) and maximum (SR_{max}) values for each paired horizon by using the propagating individual errors applied to our throw, dip, and age data through equations 1-3. To highlight uncertainty in slip-rate values, we present the preferred, minimum and maximum values where referencing slip rate in the text, and use the minimum and maximum slip rate values as error bars in any plots. Despite the uncertainties, the seismic reflection dataset allows us to explore the spatial-temporal evolution of slip rate at 100 m intervals along each fault, providing useful insights into the long-term evolution of faults and fault networks.

3.1 Modelling earthquake rates

To investigate the effect of variable slip rate and changes in fault length observed across the studied fault network we use the MATLAB package FiSH (Pace et al., 2016), to calculate the expected earthquake occurrence rates across four time periods (209.5 to 192 Ma, 192 to 170

Ma, 170 to 142.3 Ma, and 142.3 to 137.3 Ma) for two examples: 1) a single fault with a relatively simple geometry (i.e., limited sinuosity and no hard linkage to nearby faults); and 2) a fault network that includes the single fault (see Table S4.1 for input parameters). FiSH derives expected earthquake rates based on fault data such as fault length, slip-rate, fault dip, seismogenic thickness, and established empirical relationships (Pace et al., 2016). For fault dip and slip-rate we take the arithmetic mean of all picks along a given fault, using rift average dip to limit horizon specific errors. The along-fault length (i.e. considering the presence of fault bends, not tip-to-tip length) is extracted based on slip-rate profiles. FiSH requires the seismogenic thickness (aka depth extent of the fault) to be input to calculate the area of the fault surface. We take a slightly different approach herein because (a) faults may extend below the surveyable depth and (b) we cannot constrain the seismogenic thickness when these faults were active. Instead, to calculate the depth extent of the faults, we assume faults have a constant length to height aspect ratio of 2.15 (Nicol et al., 1996), although we note that a wide range of fault aspect ratio values exist (Roche et al., 2013; Soliva et al., 2006; Torabi & Berg, 2011). This approach was adopted instead of using a consistent fault width (e.g., extending to the seismogenic thickness of the crust), which would lead to unrealistic fault surface geometries, particularly for short faults. If these assumptions are incorrect, and the faults have larger or smaller aspect ratios, then the resultant earthquake magnitudes would be higher or lower respectively. Although the studied faults are not presently active, our aim is to constrain how earthquake rates change as the slip rates within a fault network changes over different time periods and to investigate how earthquake occurrence could vary.

4 Results

4.1 Single fault (Fault 1)

To first investigate how slip rates vary along a single fault through time, we choose a single fault (Fault 1) that is physically (if not mechanically and kinematically) isolated from other nearby faults and is relatively geometrically simple (i.e. limited changes in strike and dip). We extract total displacement over the total lifetime of the rift (Figure 3a), as well as displacement over four different time periods (Figure 3b-e). For the four time periods, the displacement is converted to slip rate using the ages of the offset horizons (see Figure 2d for the age framework).

Considering the total displacement (Figure 3ai), the displacement profile has higher displacement in the centre of the fault, with a slight skew to the northern end of the fault, and lower displacement at the fault tips.

The slip rate in four different time periods is calculated and plotted in map-view (Figure 3b-e, i) and as distance along the fault (Figure 3b-e, ii). Slip is recorded along the full length of

the fault for all time periods, suggesting the fault established its length within the first time period (i.e., following a constant-length model of fault growth (e.g., Childs et al., 2017; Rotevatn et al., 2019; Walsh et al., 2002). Across the different time periods, the magnitude of slip rate is variable over the rifting period. Between the first (209.5-192 Ma, Figure 3b) and second periods (192-170 Ma, Figure 3c), the slip rate on the fault decreases, with the maximum slip rate remaining constant $0.0054^{+0.001}_{-0.0008}$ mm/yr to $0.0053^{+0.0018}_{-0.0011}$ mm/yr, and no discernable change in mean slip rate $0.0023^{+0.0009}_{-0.0007}$ mm/yr to $0.0026^{+0.0008}_{-0.0007}$ mm/yr. The second and third time periods (170-142.3 Ma, Figure 3c) are also characterised by a decrease in slip rate, with the maximum slip rate reducing from $0.0053^{+0.0018}_{-0.0011}$ mm/yr to $0.0029^{+0.0009}_{-0.0007}$ mm/yr, and the mean slip rate approximately halving from $0.0026^{+0.0008}_{-0.0007}$ mm/yr to $0.0013^{+0.0006}_{-0.0005}$ mm/yr. The final period (142.3-137.3 Ma, Figure 3e) contrasts with earlier ones, in that the slip rate increases by an order of magnitude, with the maximum slip rate increasing from $0.0029^{+0.0009}_{-0.0007}$ mm/yr to $0.046^{+0.012}_{-0.006}$ mm/yr, and the mean slip rate from $0.0013^{+0.0006}_{-0.0005}$ mm/yr to $0.016^{+0.004}_{-0.006}$ mm/yr.

In addition to variability in the magnitude of maximum and mean slip rate, the shape of the along-strike slip rate profile also varies with time (Fig 3). The position of maximum slip rate measured along the fault changes over time (indicated on Figure 3b-e, i), but these may be localised maxima relating to a single point on the fault (e.g. Figure 3di). However, variations are also observed in the overall shape of the slip-rate profile (Figure 3b-e, ii). For example, the slip rate profiles are less skewed towards the northern end of the fault in the first two periods (Fig. 2b-c,ii), whereas in the third period, the profile is more elliptical than triangular (Fig. 2dii). In the final period, the shape of the profile (Fig. 2eii) is similar to the long-term profile (i.e. the whole rifting phase, Figure 3aii); this is likely because the higher slip rate (~10x times greater than other time periods) in the final time period has a large impact on the long-term profile.

4.2 Fault network

Fault 1 occurs within a fault network comprising nine faults, some of which are physically linked (Figure 4a). One fault, Fault 7 is perpendicular to the other nine faults and we therefore omit it from our analysis of along-strike trends across the fault network (Figure 4a).

Considering the total displacement across the network, many of the faults show higher throw near their centres across all time periods (e.g., Faults 1, 4 and 8; Figure 4ai). Note that due to the ~2.5 km section of Fault 4 that shows no slip during the earliest time period (Figure 4b), this fault is characterised by multiple strands during this period (Figure 4b). During all subsequent time periods, slip is evidenced across the full fault trace, suggesting the tips of initially isolated strands grew and coalesced to form a single structure by 192 Ma (Figure 4c). The cumulative throw across each individual fault over the four periods studied is plotted in

Figure 4aii, as well as the total along-strike throw profile (which sums the throws perpendicular to the orientation of the network).

Along-strike profiles of slip rate for each fault are plotted for each period, with the profiles for individual faults aligned for easy across-strike comparison. While complex, there are several key observations. First is that, like for the single fault, the magnitude of slip rate of individual faults and the entire fault network varies over time, and that all faults increase their slip rate in the final period (142.3-137.3 Ma, note the different vertical scale in Figure 4e). Second, the shape of the along-strike slip rate profile varies for individual faults over time; for example, Fault 2 has a profile that is relatively flat in the first two periods (209.5-192 Ma and 192-170 Ma, Figure 4b and c), near-triangular in the third period (170-142.3 Ma, Figure 4d), and skewed towards its northern end in the final period (142.3-137.3 Ma, Figure 4e). In addition to the variable slip rate profile on individual faults, the shape of the cumulative or summed profile varies over time; for example, in the third period, slip is skewed towards the southern end of the fault network (Figure 4d).

We select six transects through the fault network, orientated approximately perpendicular to its overall trend, to study how the slip rate varies over time and throughout the fault network. For the transects, we can investigate variations in slip rate with a higher temporal resolution, resolving all eight time periods shown in Figure 2d. The location of transects was chosen such that temporal variation in slip rate can be explored at key along-strike locations, capturing different faults and encompassing a different number of across-strike faults (Figure 5a). In all transects, the rapid acceleration of slip rate towards the end of rifting can be seen in Figure 5bi, consistent with the observations from the single fault.

For each transect (Figure 5c-h), the slip rate on each individual fault is measured and plotted over time (Figure 5c-h, i). To enable comparison and to investigate how the dominance of different faults changes over time, we calculate and plot the percentage of total slip rate accommodated on each fault across the transect (Figure 5c-h, ii). This indicates how the extension is being shared across the fault network, and whether this remains constant or varies over time.

Whereas the magnitude of slip rate varies through time across all transects, another key observation is how the dominance of different faults changes, as seen on all transects (Figure 5c-h, ii). For example, in Transect 1, Fault 8 accommodates the majority (i.e., >50%) of the deformation from 200-192 Ma and 181-137.3 Ma, whereas Fault 9 is dominant from 209.5-200 Ma and 192-181 Ma. A similar pattern can be seen in Transect 3 (the other transect with only two faults across strike), with Fault 1 being dominant from 209.5-192 Ma and 181-140 Ma, and

Fault 5 from 192-181 Ma and 140-137.3 Ma. Where there are more than two faults across strike (i.e., all other transects), the patterns of dominance between the faults are more complex, with: (1) faults sharing the extension approximately equally, e.g. Transect 4, 170-142.3 Ma (Figure 5f.i.i.), or (2) two out of three faults taking up the extension, e.g. Transect 2, 181-142.3 Ma, during which time Fault 9 is not slipping (Figure 5dii), or (3) one fault being dominant (e.g. Transect 6, Fault 4 accommodating 70% of extension during 209.5-200 Ma and 92% of extension during 181-175 Ma, with Fault 2 taking-up 92% of extension during 200-192 Ma (Figure 4hii)). This demonstrates that the way that extension is shared across a normal fault network is complex and varies through time, with activity and dominance switching between faults.

4.3 Variations in earthquake rates due to slip rate variations

The cumulative annual earthquake occurrence rates of individual faults (Fig 6a) and the fault network (Fig S4.2; S4.4) were calculated using fault properties extracted across the full time window (i.e., 209.5 to 137.3 Ma), and the four-time intermediate time intervals investigated in this study (Table S3). Similarly to other faults across the Exmouth Plateau (Lathrop et al., 2021), we observe fault length to be established quickly across most faults, and therefore for most faults we use the same fault length for all time intervals. An exception to this is sections of F4, and the tips of F2, that show no slip during the 209.5 to 192 ma time period (Fig 4b, c), suggesting these faults grew between the first two time periods. To account for this, we split F4 into F4a and F4b during the 209.5 to 192 Ma time period and calculate earthquake occurrence rates for each section separately, while using different lengths of F2 in the first and subsequent time periods. To compare different time windows, recurrence intervals for earthquakes with Mw > 4.0 (Table S4.2) and Mw > 5.0 (Table S4.3) were calculated by taking the inverse of their annual cumulative rates, these magnitudes were chosen because all faults in the system can produce a M>4 earthquake (based on scaling laws) and to ensure that recurrence interval variations are consistent. This calculation assumes that individual faults partially or completely rupture, and multi-fault ruptures are not considered. In this study, we are primarily interested in the variation of the calculated recurrence intervals, rather than the absolute values, because the studied faults studied are presently inactive.

4.3.1 Earthquake rates on Fault 1

For Mw > 5.0 earthquakes on Fault 1, the recurrence interval calculated using time-averaged slip rate (i.e., 209.5 to 137.3 Ma) is 27,900 years; however, this differs from recurrence intervals calculated using intermediate horizons (Table S4). Similar recurrence intervals were calculated for the 209.5 to 192 Ma (35,700 years) and 192 to 170 Ma (31,900 years) time periods, before rates increasing by a factor of two during the 170 to 142.3 Ma time

period (68,600 years), and decrease by a factor of 10 in the final time period (142.3 to 137.3 Ma, 4,380 years). Similar trends are also observed for Mw > 4.0 earthquakes (Table S4.2). The chosen time window that slip-rate is calculated over therefore has a large effect on recurrence rates. For example, earthquake rates calculated using slip-rate extracted from the 3rd time interval would underestimate the seismic hazard in the following 4th time interval, and the use of time-average slip-rate could either over-, or under- estimate the recurrence times of damaging earthquakes when compared to using rates calculated using intermediate horizons.

4.3.2 Earthquake rates across the fault network

The recurrence time and cumulative earthquake rates across the fault network depend on the time period of interest, and the earthquake magnitude (Fig 6b, c). Similarly to Fault 1, the recurrence interval of M>5 earthquakes calculated using rift averaged slip rates (7,820 years) differs from individual time periods (Table S4), and a reduction in recurrence intervals of M>5 across the fault network from 12,200 to 977 years occurs during the final time period (142.3 to 137.3 Ma; Fig 6b, Table S3-4). During the first three time periods (i.e., 209.5 to 142.3 Ma), the recurrence intervals of M>5 (11,000 to 13,100 years; Table S4) and M>4 (760 to 952 years; Table S3) earthquakes are similar, with the cumulative earthquake rate curves closely spaced at lower magnitudes (Fig 6a, S4.4). However, at magnitudes above 5.5, earthquake rates are lower during the 170 to 142.3 Ma time period, when compared to preceding time periods, coinciding with a deceleration in the three longest faults in the network (F5, F8, F9; Table S2).

Where the recurrence rates on individual faults are considered, recurrence rates show a high degree of variation between time intervals (Figure 6c, Fig S4.1, Table S4.2-S4.3), even where rates across the whole network remain similar (Fig 6c). For example, comparing the 209.5 to 192 Ma time period, where recurrence rates of M>5.0 earthquakes are 13,100 years, to the 170 to 142.3 Ma time period, where recurrence rates across the network are 12,200 years, the difference in rates between time windows on individual faults range from 32,900 years (F1) to 649,000 years (F4). These differences mean that the contribution of earthquake rates differ across the network, depending on the fault and time period. Some faults contribute similarly to the earthquake rate across different time periods, for example Fault 1 which contributes 28% to the cumulate rate of M>5.0 earthquakes using the rift averaged slip-rate and between 18% (170 to 142.3 Ma) and 37% (209.5 Ma to 192 Ma) using intermediate time windows. Conversely, some faults such as Fault 4 vary considerably between time periods, which contributes 9% to the cumulate rate of M>5.0 earthquake using the rift averaged slip-rate, but ranges from 2% (209.5 to 192 Ma) to 32% (170 to 142.3 Ma).

In addition to slip-rate, fault length also affects how earthquake rates are distributed across the fault network (Table S4.2, S4.2, S4.4). Firstly, three of the studied faults were too

small to generate M>5 earthquakes (Faults 3, 6, 7; Table S4.1, Fig S4.4), and therefore the effect of these faults is only observed when recurrence rates of M>4.0 earthquakes are considered (Fig S4.1). Whilst Faults 3 and 6 contribute similarly to the fault network across all time periods (1 to 4% and 1 to 2% respectively), Fault 7 contributes 21% for M>4.0 earthquakes during the first two time periods, before dropping to 4% in 170 to 142.3, and 1% in 142.3 to 137.3 Ma. This highlights that although similar patterns are observed for M>4.0 earthquakes, the relative proportion across the network is not identical to M>5.0, and different faults can contribute more to the recurrence rates of different magnitude earthquakes (Fig S4.4. Table S4.2, S 4.3). Where slip-rate decreases on a longer fault (e.g., Fault 5), this will have a greater impact on M>5 earthquakes when compared to changes in slip-rate on shorter faults (e.g., Fault 2). Additionally, where a fault lengthens between time intervals (e.g., Fault 4, Fig 4), the recurrence time of larger earthquakes can decrease, even where the slip-rate across these time intervals remains similar (Fig 6, Table S4.1). Therefore, both the spatial distribution and frequency of damaging earthquakes (M>5.0) across the network can vary through time depending on the distribution of slip-rate across the network, and the length of the faults which accommodate the majority of the slip during a given time period.

5 Discussion and implications

5.1 Temporal slip rate variability

Our data reveals temporal variability in slip rates across individual faults and the fault network (Figs 3, 4, 5). Although the absolute slip rates are relatively low when compared to those in global compilations (Nicol et al., 1997), they are consistent with slip rates extracted from other normal faults on the NW Shelf of Australia (Andrews et al., 2024; Lathrop et al., 2021; Pan et al., 2022). Despite being relatively low, slip-rates across the study area vary by up to an order of magnitude across the studied time period (Figs 3-5), suggesting temporal slip-rate variability should be considered when reconstructing fault histories.

Slip-rate variations are observed across a diverse range of tectonic settings and time periods (e.g., Dolan et al., 2007; Friedrich et al., 2003; Gauriau & Dolan, 2021; McClymont et al., 2009; Nicol et al., 2016). Comparing these variations across different faults and tectonic settings requires a consistent metric. A common value for quantifying earthquake variability in seismic hazard studies is the Coefficient of Variation (CV, the standard deviation of recurrence times divided by the mean recurrence time). However, faults with different slip histories can yield identical CVs, since the metric captures only the variability on the recurrence intervals and not the sequence of events nor the magnitude of slip (Cowie et al., 2012). They proposed a measure of slip-rate variability by calculating the ratio between the standard deviation of slip rate over a sliding time window to the mean slip rate. Although this metric is argued by the

548 authors to be a more robust indicator of variability in slip histories, it requires a continuous slip-
549 history, which is often unavailable due to non-uniform time windows over which slip rates are
550 calculated (e.g., Lathrop et al., 2021; Meyer et al., 2002; Nixon et al., 2024; Weldon et al.,
551 2004). Gauriau and Dolan (2021) suggested calculating slip-rate variability by dividing the
552 fastest slip-rate by the slowest, but this returns very high values for intercontinental faults with
553 large differences between maximum and minimum rates, or infinite values of slip-rate
554 variability for faults with periods of quiescence (Table S6.1). This makes comparing variability
555 between faults across different tectonic settings challenging. To overcome these limitations, we
556 introduce a new measure, termed the normalised slip-rate variability (NSRV), defined as the
557 range (maximum rate – minimum rate) in slip-rate divided by the slip-rate averaged over the
558 studied time interval (i.e. total slip divided by total time, which is thousands to millions of
559 years). Calculating NSRV for individual faults, or the fault network as a while, offers a simple yet
560 robust metric for quantifying slip-rate variability in diverse geological contexts.

561 We compiled incremental slip histories for time periods >10 kyrs (i.e. covering multiple seismic
562 cycles) for 151 faults from the literature and this study, and calculated their corresponding
563 normalised slip-rate variability (NSRV) (Fig 7, Table S6.4). For individual faults in our study, NSRV
564 values range from 1.7 to 14.4 (average = 7.1), with the whole fault network having a value of
565 6.7 (Table S6.2). This is notably higher than most published examples (range = 0.8 to 8.4,
566 average = 1.9). The elevated NSRV from our study is partly driven by a rapid acceleration in slip
567 rate across the network during the final time period considered (i.e. between 142.3 and 137.3
568 Ma, Fig 5). However, if we disregard the final time period (Figure 7b; Table S6.3), NSRV across
569 the full network is low (NSRV = 0.6); although individual faults still show a wide range in NSRV
570 values (NSRV = 0.4 to 8.1, Average = 1.9). This is because the proportion of slip accommodated
571 by a particular fault during a specific time period does not remain constant (Fig 4, 5), causing a
572 large range between maximum and minimum slip-rates and therefore a high NSRV. This
573 highlights that, like in active systems such as the Central Apennines (Faure Walker et al., 2012;
574 Pesci et al., 2009), temporal variations in strain accommodation on individual faults can occur
575 even where the strain across the network remains constant.

576 Analysis of the global dataset reveals that NSRV is largely unaffected by the duration over which
577 it is measured, with faults that have been active for < 1 Myr having an average NSRV of 1.8,
578 whereas those > 1 Myr averaging 2.0. Fault length does not appear to influence NSRV, with a
579 wide NSRV range of values being observed across both long and short faults (Fig 7b). However,
580 NSRV differs by fault type, with normal faults showing higher NSRV (2.0, n = 116) compared to
581 strike-slip faults (1.4, n = 27), although there is insufficient data to assess thrust faults (2.5, n =
582 8). The consistently high NSRV values across timescales and fault lengths suggests slip-rate
583 variability is an intrinsic feature of fault growth, with normal faults exhibiting particularly
584 irregular behaviour. This result differs from the findings of Mouslopoulou et al. (2009), who

585 show that displacement rates generally display a greater range for smaller faults and over
586 shorter time periods. They further suggest that, provided the fault system strain rates are
587 uniform, displacement rates stabilise over timescales of 20 to 300 kyr. In contrast, our NSRV
588 index is calculated for individual faults and quantifies temporal variability in slip rate on a fault-
589 be-fault bases across the time period data is available for, rarther than absolute rates across
590 different time periods. In our dataset, we do not observed a reduction in NSRV for time
591 windows greater than 20 to 300 kyr, and instead find slightly higher values where durations
592 exceed 1 Myr (Figure 7). While shorter sampling intervals may give a greater range in absolute
593 slip rate than longer intervals, our results suggest that individual faults exhibit comparable
594 degrees of temporal variability across a wide range of timescales.

595 Several mechanisms have been proposed to explain long-term (million-year) changes in slip-
596 rate on normal faults, including strain localisation onto border faults during rift evolution
597 (Meyer et al., 2002; Nixon et al., 2024; Walsh et al., 2003), variable plate velocities (Nicol et al.,
598 2005), and incremental slip rate due to fault-segment linkage (Cartwright & Mansfield, 1998;
599 Cartwright et al., 1995) Our study area, which is <20 km wide, does not image border faults and
600 shows no evidence for localisation onto larger faults over the studied time period, with slip
601 accrued on all faults across all time periods (Figure 4). Although changes in plate velocity are
602 difficult to constrain across the NW Shelf due to only half the margin being preserved (Lathrop
603 et al., 2021), no regional change has been suggested that would explain the timing and
604 magnitude of the observed slip-rate acceleration between 142.3 and 137.3 Ma (Bilal & McClay,
605 2022). Along-strike segment linkage is known to influence slip-rates during the early stages of
606 fault growth (Meyer et al., 2002; Nixon et al., 2024). However, our slip profiles show that,
607 similar to elsewhere on the Exmouth Plateau (Lathrop et al., 2021; Pan et al., 2022), all faults,
608 except Fault 4, followed the constant length model of fault growth (Childs et al., 2017; Nicol et
609 al., 2020; Rotevatn et al., 2019; Walsh et al., 2002), reaching their maximum length during the
610 209.5 to 192 Ma time window, and thus we assumed a constant fault length for the earthquake
611 rate calculations. We propose that fault network geometry, i.e. the proximity and spacing of
612 faults, appears to affect slip-rates of individual faults in the study area (Figure 4, 5) as discussed
613 further below.

614 5.2 The influence of fault network geometry on spatial-temporal slip rate variability

615 Our data shows that the location of maximum slip-rate on individual faults (Fig 3, 4), and
616 the proportion of slip accommodation on individual faults (Fig 5) varies through time,
617 supporting hypothesis 2 for both research questions posed (How does displacement
618 accumulate along a single fault over time? How does displacement accumulated across a fault
619 network over time? (Figure 1). This agrees with individual fault behaviour observed from
620 physical analogue (Mansfield & Cartwright, 2001; Schlagenhauf et al., 2008) and numerical

(Cowie et al., 2012) models of fault network growth. However, the summed slip-rate profile is more supportive of hypothesis 1 (Fig 4), with the position of maximum slip-rate being fixed near the centre of the fault, apart from between 170 Ma and 142.3 Ma, when a southwards shift of ~5km occurs due to an increase in the slip rates of Faults 2 and 4 (Fig 4d). This suggests that while the distribution of strain across the network remains consistent, how that strain is partitioned between faults varies between time periods. Similar observations of faults accommodating variable proportions of displacement have been documented in the Italian Apennines and central Greece for much shorter timescales, where cosmogenic dating reveals spatial-temporal slip-rate changes during the last 15 kyr (Benedetti et al., 2013; Cowie et al., 2017; Iezzi et al., 2021; Mildon et al., 2022; Roberts et al., 2024, 2025; Sgambato et al., 2025). Over this 15 kyr timescale, regional strain across the Apennines is assumed to have remained stable (Faure Walker et al., 2012), with stress transfer between faults and underlying shear zones invoked as the cause of slip-rate changes (Mildon et al., 2022). It is unlikely that the physical mechanisms hypothesised for central Italy are applicable to our dataset, given the difference in timescales and length scales. However, these observations highlight the need to account for both the growth of individual faults and the overall distribution of strain when assessing fault network evolution.

Fault interactions play a key role in the distribution and evolution of slip on faults within a fault network by producing local stress concentrations and perturbations that affect the geometry, kinematics, and earthquake rupture patterns of interacting faults (e.g., Fossen et al., 2005; Kattenhorn et al., 2000; Nixon et al., 2014a; Peacock et al., 2017; Rodriguez Piceda et al., 2025). Interactions can occur on geometrically linked faults, which are physically connected by a branch line, and/or kinematically linked, where slip patterns on two or more faults are complimentary (e.g., Nicol et al., 2020; Nixon et al., 2024; 2014a; Peacock et al., 2017). The network studied herein shows a combination of both interaction types (Fig 4ai), with the arrangements of faults having a direct effect on slip accumulation. We find greater variability in the proportion of slip on individual faults where multiple faults are arranged across-strike (e.g., Transects 4-6; Figure 5f-h). Even where only two across-strike faults are present, strain and stress transfer occurs (e.g., Figure 5c). Similar patterns, though over very different spatial scales, have been documented in the Italian Apennines, where less variability is observed in the Southern Apennines in a location where faults are predominantly arranged along-strike from each other, when compared to the Central Apennines, where faults are predominantly arranged across strike. At the millennial scale of the earthquake cycle, across-strike faults are known to exhibit complex slip behaviours, including partial ruptures, slow-slip events, and earthquake arrest (Mia et al., 2024; Romanet et al., 2018; Yin et al., 2023), with across-strike offsets having a greater effect when compared to along-strike geometries (Rodriguez Piceda et al., 2025). While our slip-rate values cover multiple earthquake cycles, our data suggests that

overlapping across-strike fault geometries can continue to influence slip-rate variability over substantially longer million year timescales.

Consistent with previous studies (e.g., Cowie et al., 2012; Gauriau & Dolan, 2021), our findings underscore the role of structural complexity in driving slip-rate variations across multiple time scales. We find greater NSRV values for normal faults, which form as part of faults networks within continental rifts (Fig 7). Rift systems are characterised by many faults arranged in an across-strike geometry (e.g., Duffy et al., 2017; Scholz & Contreras, 1998), promoting stress interactions between faults and complex earthquake behaviour (Rodriguez Piceda et al., 2025). Conversely, strike-slip faults are predominantly arranged in an along-strike arrangement, with slip occurring roughly parallel to fault strike (e.g., Sylvester, 1988; Woodcock, 1986) and thrust faults often localise onto discrete slip planes at a low angle to the compression direction (e.g., Ellis & Dunlap, 1988). In these cases, stress interactions will be lower and have a different pattern, although not absent particularly in areas of variable fault and fault network geometries (Lin & Stein, 2004; Peacock et al., 2017). The arrangement of normal faults likely explains the higher NSRV values for normal faults (Fig 7), and why areas of continental extension display such variable slip-rates when compared to other plate boundary systems. Overall, our results reinforce the need to consider fault network geometry, and the effect this may have on fault interactions, when evaluating fault growth and suggest that seismic hazard models that do not consider the whole network may miss critical dynamics inherent to fault networks.

5.3 Implications of slip rate variability for seismic hazard assessment

Active fault systems are characterised by temporal variations in slip-rate variability (Iezzi et al., 2020; McClymont et al., 2009; Nicol et al., 2006; Nixon et al., 2024; Roberts et al., 2024, 2025; Sgambato et al., 2025), leading to corresponding variations in earthquake recurrence, and thus highlighting the need for time-dependent seismic hazard assessments (Dahm & Hainzl, 2022; Verdecchia et al., 2019). In our study, slip-rates fall in the lower end of the expected range for normal faults relative to known faults and their slip rates (Nicol et al., 1997), leading to recurrence intervals for Mw > 5 earthquakes of ~4,000 to ~63,000 years on the single fault, substantially longer than the hundreds to thousands of years typically observed in actively extending regions (e.g. Greece, central Italy, Basin and Range, USA (Console et al., 2013; Galli, 2020; Schwartz & Coppersmith, 1984)). Despite this, the magnitude of slip-rate variability from our study is comparable to other active extensional systems (Figure 7 for comparison). Probabilistic Seismic Hazard Assessment (PSHA) typically relies on single, time-averaged slip-rates derived from geological data (e.g., Pace et al., 2016; Williams et al., 2023), which can include some temporal variations in slip rate, but which do not fully explore their impact. Where time-dependence is incorporated, usually through Coulomb stress modelling, it often relies on short historical and/or instrumental records (e.g., Chan et al., 2017; Dahm & Hainzl,

2022; Toda et al., 1998; Verdecchia et al., 2019). Both data types have limitations: geological records rarely resolve long-term (>100 kyr) variability (Cowie et al., 2012), while instrumental and historical datasets are often too short and incomplete to span full seismic cycles (Mäntyniemi et al., 2014; Swafford & Stein, 2007). By comparing slip-rates calculated across multiple time windows (Figure 4, 5), we show how the width of the time window will affect earthquake rates. For example, on Transect 3, slip acceleration initiates during the 142.3–140 Ma interval and intensifies during the 140–137.3 Ma interval. Averaging across the full 142.3–137.3 Ma window would therefore overestimate hazard in the earlier part of the interval and underestimate it in the latter. This demonstrates that slip-rate inputs must be derived from time windows long enough to capture clustered or transient behaviour (e.g., Friedrich et al., 2003), yet not so long that they obscure meaningful long-term variability. Although driven by different mechanisms, this behaviour mirrors evidence from active systems such as the Corinth Rift in Greece, where fault linkage and localisation onto major structures are associated with fault-specific slip rates over the past 2 Myr, with significant changes occurring as recently as 130 ka (Nixon et al., 2024). Our findings reinforce the importance of characterising slip-rate variability across relevant timescales and quantifying the uncertainty introduced when long-term rates do not reflect present-day fault behaviour.

In addition to temporal changes in recurrence rates, the spatial distribution of hazard also varies as different faults in the system accommodate strain at different times. Although the total rate of Mw > 5 earthquakes across the network remains similar up to 142.3 Ma (~10,000 years, Figure 6c), the rates on individual faults differ. For instance, Fault 9 has the highest Mw > 5 earthquake rates between 192 and 209.5 Ma, whereas Faults 2 and 4 became more active later, between 142.3 and 170 Ma. This southward migration of elevated earthquake rates by > 10 km illustrates that changes in fault-specific slip rates can alter the rates of damaging earthquakes at a specific location, even if regional strain rates remain constant. Similar behaviour is observed in active regions such as the Central Apennines, where slip-rate variability is spatially complex, especially where multiple faults are arranged across strike from each other (Roberts et al., 2024; Rodriguez Piceda et al., 2025; Sgambato et al., 2023). This suggests that time-dependant PSHA needs to consider not only short term factors that cause earthquake clustering, but also how the long-term slip rate behaviour of faults within the network may evolve differently. One way to address this is by testing the effects of the spatio-temporal variability of long-term slip-rate on earthquakes rates with physics-based earthquake simulators (e.g. Herrero-Barbero et al., 2023; Shaw et al., 2018).

In addition to changes in absolute slip-rate, we observe changes in the shape of slip-rate profiles between faults and time periods. Faure Walker et al. (2019) show that spatially variable slip rate and, specifically, assumptions about the slip rate profile shape (e.g., triangular vs. boxcar) can alter calculated strain rates by a factor of 0.5 to 1.5 and change calculated

731 earthquake occurrence rates by 100s of years (from 262-524 years in their published example).
732 In our analysis, the overall network slip-rate profile is similar in three of the four main time
733 intervals (Figure 4bii, cii, eii), but it differs markedly during 170 to 142.3 Ma (Figure 4dii). At the
734 level of an individual fault, displacement profiles exhibit large variation in shape, including
735 multiple peaks and troughs (Figure 4). This contrast with the smoother, time-average slip rate
736 profile (e.g., Figure 4aii). As a result, estimates of earthquake rates using the "time-averaged"
737 slip-rate profile could diverge significantly from those derived using the slip-rate profiles of
738 individual faults (Figure 4b-e). Slip rates derived over time periods up to ~10 times a fault's
739 average recurrence interval provide important constraints for seismic hazard assessments. Our
740 analysis of million-year slip rates demonstrates that changes in both the magnitude and spatial
741 distribution of slip rate across individual faults and the wider fault network directly impact
742 calculated earthquake recurrence rates and how these are partitioned across the network
743 (Figure 4, 6). As we observe high NSRV across time windows of ~10,000 years (Figure 7), we
744 suggest that similar variability is likely to influence seismic hazard assessments at shorter
745 timescales. As a result, our findings highlight the potential limitations of spatial and temporal
746 averaging and underscore the importance of incorporating fault-specific, time-dependent slip-
747 rate variability into seismic hazard models, particularly in fault networks containing multiple
748 faults arranged across-strike from each other.

749 **5 Conclusions**

750 In this study, we used high-resolution 3D seismic reflection data to quantify how slip
751 rates evolve along and across a network of normal faults over a ~70 Myrs. Our results reveal
752 substantial spatial and temporal variability in slip rate, even on faults with relatively simple
753 geometries. Along-strike slip-rate profiles change shape through time, and rates can vary by up
754 to two orders of magnitude, indicating that single-point measurements may underrepresent
755 the complexity of fault behaviour. Across the fault network, slip is not consistently partitioned,
756 with different faults dominating at different time periods and the location of maximum slip
757 changing through time. These patterns suggest that fault interactions and network geometry
758 play a key role in controlling the distribution of strain within a fault network at million-year
759 timescales.

760 By calculating earthquake recurrence rates, we find that the summed rates of Mw >5
761 earthquakes remained consistent across the first three time periods, prior to reducing by
762 reducing by an order of magnitude to ~1000 years during the 142.3 to 137.3 Ma time period.
763 We find that while summed rates may remain consistent, the contributions from individual
764 faults vary markedly between time intervals. By considering which faults are contributing to the
765 summed rates, the dominant faults move from the north to the south of the fault network. This
766 highlights that the spatial distribution of large earthquakes could differ between different time

767 periods. Our study demonstrates the importance of considering fault network geometry when
768 undertaking seismic hazard assessments or building tectonic models.

769 **Acknowledgments**

770 We would like to thank DugInsight for the provision of an academic license for their software
771 package. We thank Francesco Visini for his help to begin the FiSH modelling. This work was
772 supported by a UKRI Future Leaders Fellowship MR/ T041994/1 (PI - Z. Mildon).

773 **Open Research**

774 Version .5.1 (2021) of DUG Insight software used for seismic visualisation,
775 interpretation and alaysis is preserved at http://www.dug.com, available via
776 academic licsence and developed openly at http://www.dug.com.

777 The seismic reflection and well data used to interpret the long term slip rate
778 variability in the study are available at Geoscience Australia and can be accessed
779 through the National Offshore Petroleum Information Management System
780 (NOPIMS) via https://nopims.dmp.wa.gov.au/nopims

781

782

783 **Conflict of Interest Disclosure**

784 "The authors declare there are no conflicts of interest for this manuscript."

785 **References**

786 Alcalde, J., Bond, C. E., Johnson, G., Ellis, J. F., & Butler, R. W. H. (2017). Impact of seismic image
787 quality on fault interpretation uncertainty. GSA Today. https://doi.org/10.1130/GSATG282A.1

788 Allen, P. A., & Allen, J. R. (2013). Basin Analysis: Principles and Application to Petroleum Play
789 Assessment. John Wiley & Sons.

790 Andrews, B. J., Mildon, Z. K., Jackson, C. A. L., & Bond, C. E. (2024). Quantifying fault
791 interpretation uncertainties and their impact on fault seal and seismic hazard analysis. Journal
792 of Structural Geology, 184, 105158. https://doi.org/10.1016/j.jsg.2024.105158

793 Barrett, B. J., Hodgson, D. M., Jackson, C. A. -L., Lloyd, C., Casagrande, J., & Collier, R. E. Ll.
794 (2021). Quantitative analysis of a footwall-scarp degradation complex and syn-rift stratigraphic
795 architecture, Exmouth Plateau, NW Shelf, offshore Australia. Basin Research, 33(2), 1135–1169.
796 https://doi.org/10.1111/bre.12508

797 Benedetti, L., Finkel, R., Papanastassiou, D., King, G., Armijo, R., Ryerson, F., et al. (2002). Post-
798 glacial slip history of the Sparta fault (Greece) determined by 36Cl cosmogenic dating: Evidence
799 for non-periodic earthquakes. Geophysical Research Letters, 29(8), 87-1-87–4.
800 https://doi.org/10.1029/2001GL014510

801 Benedetti, L., Manighetti, I., Gaudemer, Y., Finkel, R., Malavieille, J., Pou, K., et al. (2013).
802 Earthquake synchrony and clustering on Fucino faults (Central Italy) as revealed from in situ
803 36Cl exposure dating. Journal of Geophysical Research: Solid Earth, 118(9), 4948–4974.
804 https://doi.org/10.1002/jgrb.50299

805 Bilal, A., & McClay, K. (2022). Tectonic and stratigraphic evolution of the central Exmouth
806 Plateau, NW Shelf of Australia. Marine and Petroleum Geology, 136.
807 https://doi.org/10.1016/j.marpetgeo.2021.105447

808 Bilal, A., McClay, K., & Scarselli, N. (2020). Fault-scarp degradation in the central Exmouth
809 Plateau, North West Shelf, Australia. Geological Society, London, Special Publications, 476(1),
810 231–257. https://doi.org/10.1144/SP476.11

811 Black, M., McCormack, K. D., Elders, C., & Robertson, D. (2017). Extensional fault evolution
812 within the Exmouth Sub-basin, North West Shelf, Australia. Marine and Petroleum Geology, 85,
813 301–315. https://doi.org/10.1016/j.marpetgeo.2017.05.022

814 Bond, C. E. (2015). Uncertainty in structural interpretation: Lessons to be learnt. Journal of
815 Structural Geology, 74, 185–200. https://doi.org/10.1016/j.jsg.2015.03.003

816 Brown, A. R. (2011). Interpretation of Three-Dimensional Seismic Data (7th ed.). American
817 Association of Petroleum Geologists, Tulsa, Oklahoma, U.S.A..

818 Brune, J. N. (1968). Seismic moment, seismicity, and rate of slip along major fault zones. Journal
819 of Geophysical Research (1896-1977), 73(2), 777–784.
820 https://doi.org/10.1029/JB073i002p00777

821 Cartwright, J. A., & Mansfield, C. S. (1998). Lateral displacement variation and lateral tip
822 geometry of normal faults in the Canyonlands National Park, Utah. Journal of Structural
823 Geology, 20(1), 3–19. https://doi.org/10.1016/S0191-8141(97)00079-5

824 Cartwright, Joseph A., Trudgill, B. D., & Mansfield, C. S. (1995). Fault growth by segment linkage:
825 an explanation for scatter in maximum displacement and trace length data from the
826 Canyonlands Grabens of SE Utah. Journal of Structural Geology, 17(9), 1319–1326.
827 https://doi.org/10.1016/0191-8141(95)00033-A

828 Chan, C., Wang, Y., Wang, Y., & Lee, Y. (2017). Seismic-Hazard Assessment over Time: Modeling
829 Earthquakes in Taiwan. Bulletin of the Seismological Society of America, 107(5), 2342–2352.
830 https://doi.org/10.1785/0120160278

831 Chartier, T., Scotti, O., & Lyon-Caen, H. (2019). SHERIFS: Open-Source Code for Computing
832 Earthquake Rates in Fault Systems and Constructing Hazard Models. Seismological Research
833 Letters, 90(4), 1678–1688. https://doi.org/10.1785/0220180332

834 Chellingsworth, L., Bentley, M., & Wynn, T. (2015). Human factors in seismic uncertainty —
835 Restoring a realistic uncertainty range. Interpretation, 3, SQ21–SQ32.
836 https://doi.org/10.1190/INT-2014-0203.1

837 Childs, C., Nicol, A., Walsh, J., Watterson, J. (2003). The growth and propagation of
838 synsedimentary faults. Journal of Structural Geology 25, 633-648.
839 https://doi.org/10.1016/S0191-8141(02)00054-8

840 Childs, C., Holdsworth, R. E., Jackson, C. A.-L., Manzocchi, T., Walsh, J. J., & Yielding, G. (2017).
841 Introduction to the geometry and growth of normal faults. In C. Childs, R. E. Holdsworth, C. A.-L.
842 Jackson, T. Manzocchi, J. J. Walsh, & G. Yielding (Eds.), The Geometry and Growth of Normal
843 Faults (Vol. 439, p. 0). The Geological Society of London. https://doi.org/10.1144/SP439.24

844 Childs, Conrad, Worthington, R. P., Walsh, J. J., & Roche, V. (2019). Conjugate relay zones:
845 geometry of displacement transfer between opposed-dipping normal faults. Journal of
846 Structural Geology, 118, 377–390. https://doi.org/10.1016/j.jsg.2018.11.007

847 Console, R., Falcone, G., Karakostas, V., Murru, M., Papadimitriou, E., & Rhoades, D. (2013).
848 Renewal models and coseismic stress transfer in the Corinth Gulf, Greece, fault system. Journal
849 of Geophysical Research: Solid Earth, 118(7), 3655–3673. https://doi.org/10.1002/jgrb.50277

850 Cowie, P. A., & Scholz, C. H. (1992). Growth of faults by accumulation of seismic slip. Journal of
851 Geophysical Research, 97(B7), 11085–11095. https://doi.org/10.1029/92JB00586

852 Cowie, P. A., Underhill, J. R., Behn, M. D., Lin, J., & Gill, C. E. (2005). Spatio-temporal evolution
853 of strain accumulation derived from multi-scale observations of Late Jurassic rifting in the
854 northern North Sea: A critical test of models for lithospheric extension. Earth and Planetary
855 Science Letters, 234(3), 401–419. https://doi.org/10.1016/j.epsl.2005.01.039

Cowie, P. A., Roberts, G. P., Bull, J. M., & Visini, F. (2012). Relationships between fault geometry, slip rate variability and earthquake recurrence in extensional settings: Fault geometry control on earthquake rupture. Geophysical Journal International, 189(1), 143–160. https://doi.org/10.1111/j.1365-246X.2012.05378.x

Cowie, P. A., Phillips, R. J., Roberts, G. P., McCaffrey, K., Zijerveld, L. J. J., Gregory, L. C., et al. (2017). Orogen-scale uplift in the central Italian Apennines drives episodic behaviour of earthquake faults. Scientific Reports, 7(1), 44858. https://doi.org/10.1038/srep44858

Dahm, T., & Hainzl, S. (2022). A Coulomb Stress Response Model for Time-Dependent Earthquake Forecasts. Journal of Geophysical Research: Solid Earth, 127(9), e2022JB024443. https://doi.org/10.1029/2022JB024443

Delogkos, E., Saqab, M. M., Walsh, J. J., Roche, V., & Childs, C. (2020). Throw variations and strain partitioning associated with fault-bend folding along normal faults. Solid Earth, 11(3), 935–945. https://doi.org/10.5194/se-11-935-2020

Deng, H., & McClay, K. (2019). Development of extensional fault and fold system: Insights from 3D seismic interpretation of the Enderby Terrace, NW Shelf of Australia. Marine and Petroleum Geology, 104, 11–28. https://doi.org/10.1016/j.marpetgeo.2019.03.003

Deng, H., & McClay, K. (2021). Three-dimensional geometry and growth of a basement-involved fault network developed during multiphase extension, Enderby Terrace, North West Shelf of Australia. GSA Bulletin, 133(9–10), 2051–2078. https://doi.org/10.1130/B35779.1

Direen, N. G., Stagg, H. M. J., Symonds, P. A., & Colwell, J. B. (2008). Architecture of volcanic rifted margins: new insights from the Exmouth – Gascoyne margin, Western Australia. Australian Journal of Earth Sciences, 55(3), 341–363. https://doi.org/10.1080/08120090701769472

Dolan, J. F., Bowman, D. D., & Sammis, C. G. (2007). Long-range and long-term fault interactions in Southern California. Geology, 35(9), 855–858. https://doi.org/10.1130/G23789A.1

Dolan, J. F., McAuliffe, L. J., Rhodes, E. J., McGill, S. F., & Zinke, R. (2016). Extreme multi-millennial slip rate variations on the Garlock fault, California: Strain super-cycles, potentially time-variable fault strength, and implications for system-level earthquake occurrence. Earth and Planetary Science Letters, 446, 123–136. https://doi.org/10.1016/j.epsl.2016.04.011

Duffy, O. B., Nixon, C. W., Bell, R. E., Jackson, C. A.-L., Gawthorpe, R. L., Sanderson, D. J., & Whipp, P. S. (2017). The topology of evolving rift fault networks: Single-phase vs multi-phase rifts. Journal of Structural Geology, 96, 192–202. https://doi.org/10.1016/j.jsg.2017.02.001

888 DUG Insight (version 5.1). 2021. Windows/Linux/Mac. Perth, Western Australia: DUG
889 Technology Ltd [Software] (http://www.dug.com).

890 Ellis, M. A., & Dunlap, W. J. (1988). Displacement variation along thrust faults: implications for
891 the development of large faults. Journal of Structural Geology, 10(2), 183–192.
892 https://doi.org/10.1016/0191-8141(88)90115-0

893 Etheridge, M. A., & O'Brien, G. W. (1994). Structural and Tectonic Evolution of the Western
894 Australian Margin Basin System. PESA Journal, 22.

895 Faleide, T. S., Braathen, A., Lecomte, I., Mulrooney, M. J., Midtkandal, I., Bugge, A. J., & Planke,
896 S. (2021). Impacts of seismic resolution on fault interpretation: Insights from seismic modelling.
897 Tectonophysics, 816, 229008. https://doi.org/10.1016/j.tecto.2021.229008

898 Faure Walker, J. P., Roberts, G. P., Cowie, P. A., Papanikolaou, I. D., Sammonds, P. R., Michetti,
899 A. M., & Phillips, R. J. (2009). Horizontal strain-rates and throw-rates across breached relay
900 zones, central Italy: Implications for the preservation of throw deficits at points of normal fault
901 linkage. Journal of Structural Geology, 31(10), 1145–1160.
902 https://doi.org/10.1016/j.jsg.2009.06.011

903 Faure Walker, J. P., Roberts, G. P., Sammonds, P., & Cowie, P. A. (2010). Comparison of
904 earthquake strains over 102 and 104 year timescales: Insights into variability in the seismic
905 cycle in the central Apennines, Italy. Journal of Geophysical Research: Solid Earth, 115(B10).
906 https://doi.org/10.1029/2009JB006462

907 Faure Walker, J. P., Roberts, G. P., Cowie, P. A., Papanikolaou, I., Michetti, A. M., Sammonds, P.,
908 et al. (2012). Relationship between topography, rates of extension and mantle dynamics in the
909 actively-extending Italian Apennines. Earth and Planetary Science Letters, 325–326, 76–84.
910 https://doi.org/10.1016/j.epsl.2012.01.028

911 Faure Walker, J. P., Visini, F., Roberts, G. P., Galasso, C., McCaffrey, K., & Mildon, Z. (2019).
912 Variable fault geometry suggests detailed fault-slip-rate profiles and geometries are needed for
913 fault-based probabilistic seismic hazard assessment (PSHA). Bulletin of the Seismological
914 Society of America, 109(1). https://doi.org/10.1785/0120180137

915 Fossen, H., Johansen, T. E. S., Hesthammer, J., & Rotevatn, A. (2005). Fault interaction in porous
916 sandstone and implications for reservoir management; examples from southern Utah. AAPG
917 Bulletin, 89(12). https://doi.org/10.1306/07290505041

Fossen, Haakon, & Rotevatn, A. (2016). Fault linkage and relay structures in extensional settings—A review. Earth-Science Reviews, 154, 14–28. https://doi.org/10.1016/j.earscirev.2015.11.014

Friedrich, A. M., Wernicke, B. P., Niemi, N. A., Bennett, R. A., & Davis, J. L. (2003). Comparison of geodetic and geologic data from the Wasatch region, Utah, and implications for the spectral character of Earth deformation at periods of 10 to 10 million years. Journal of Geophysical Research: Solid Earth, 108(B4). https://doi.org/10.1029/2001JB000682

Galli, P. (2020). Recurrence times of central-southern Apennine faults (Italy): Hints from palaeoseismology. Terra Nova, 32(6), 399–407. https://doi.org/10.1111/ter.12470

Gartrell, A., Torres, J., Dixon, M., Keep, M., Gartrell, A., Torres, J., et al. (2016). Mesozoic rift onset and its impact on the sequence stratigraphic architecture of the Northern Carnarvon Basin. The APPEA Journal, 56(1), 143–158. https://doi.org/10.1071/AJ15012

Gartrell, A. P. (2000). Rheological controls on extensional styles and the structural evolution of the Northern Carnarvon Basin, North West Shelf, Australia. Australian Journal of Earth Sciences, 47(2), 231–244. https://doi.org/10.1046/j.1440-0952.2000.00776.x

Gauriau, J., & Dolan, J. F. (2021). Relative Structural Complexity of Plate-Boundary Fault Systems Controls Incremental Slip-Rate Behavior of Major Strike-Slip Faults. Geochemistry, Geophysics, Geosystems, 22(11), e2021GC009938. https://doi.org/10.1029/2021GC009938

Gómez-Novell, O., García-Mayordomo, J., Ortuño, M., Masana, E., & Chartier, T. (2020). Fault System-Based Probabilistic Seismic Hazard Assessment of a Moderate Seismicity Region: The Eastern Betics Shear Zone (SE Spain). Frontiers in Earth Science, 8. https://doi.org/10.3389/feart.2020.579398

Goodall, H. J., Gregory, L. C., Wedmore, L. N. J., McCaffrey, K. J. W., Amey, R. M. J., Roberts, G. P., et al. (2021). Determining Histories of Slip on Normal Faults With Bedrock Scarps Using Cosmogenic Nuclide Exposure Data. Tectonics, 40(3), e2020TC006457. https://doi.org/10.1029/2020TC006457

Gupta, A., & Scholz, C. H. (2000). A model of normal fault interaction based on observations and theory. Journal of Structural Geology, 22(7), 865–879. https://doi.org/10.1016/S0191-8141(00)00011-0

Harris, R. A., & Simpson, R. W. (1998). Suppression of large earthquakes by stress shadows: A comparison of Coulomb and rate-and-state failure. Journal of Geophysical Research, 103(B10), 24439. https://doi.org/10.1029/98JB00793

Herrero-Barbero, P., Álvarez-Gómez, J. A., Tsige, M., & Martínez-Díaz, J. J. (2023). Deterministic seismic hazard analysis from physics-based earthquake simulations in the Eastern Betics (SE Iberia). Engineering Geology, 327, 107364. https://doi.org/10.1016/j.enggeo.2023.107364

Holden, N., Alaei, B., Skurtveit, E., & Braathen, A. (2024). Implications of depth conversion on fault geometries and fault-risk assessment in the Smeaheia CO2 storage site, northern North Sea. Geoenergy, 0(ja), geoenergy2024-006. https://doi.org/10.1144/geoenergy2024-006

Iezzi, F., Roberts, G. P., & Faure Walker, J. (2020). Throw-rate variations within linkage zones during the growth of normal faults: Case studies from the Western Volcanic Zone, Iceland. Journal of Structural Geology, 133, 103976. https://doi.org/10.1016/j.jsg.2020.103976

Iezzi, F., Roberts, G., Faure Walker, J., Papanikolaou, I., Ganas, A., Deligiannakis, G., et al. (2021). Temporal and spatial earthquake clustering revealed through comparison of millennial strain-rates from 36Cl cosmogenic exposure dating and decadal GPS strain-rate. Scientific Reports, 11(1), 23320. https://doi.org/10.1038/s41598-021-02131-3

Jackson, C. A.-L., Bell, R. E., Rotevatn, A., & Tvedt, A. B. M. (2017). Techniques to determine the kinematics of synsedimentary normal faults and implications for fault growth models. Geological Society, London, Special Publications, 439(1), 187–217. https://doi.org/10.1144/SP439.22

Karner, G. D., & Driscoll, N. W. (1999). Style, timing and distribution of tectonic deformation across the Exmouth Plateau, northwest Australia, determined from stratal architecture and quantitative basin modelling. In C. MacNiocall & P. Ryan (Eds.), Continental Tectonics (Vol. 164, pp. 271–311). London, UK: Geological Society of London. https://doi.org/10.2973/odp.proc.sr.122.1992

Kattenhorn, S. A., Aydin, A., & Pollard, D. D. (2000). Joints at high angles to normal fault strike: an explanation using 3-D numerical models of fault-perturbed stress fields. Journal of Structural Geology, 22(1), 1–23. https://doi.org/10.1016/S0191-8141(99)00130-3

Lathrop, B. A., Jackson, C. A.-L., Bell, R. E., & Rotevatn, A. (2021). Normal Fault Kinematics and the Role of Lateral Tip Retreat: An Example From Offshore NW Australia. Tectonics, 40(5), e2020TC006631. https://doi.org/10.1029/2020TC006631

Lathrop, B. A., Jackson, C. a.-L., Bell, R. E., & Rotevatn, A. (2022). Displacement/Length Scaling Relationships for Normal Faults; a Review, Critique, and Revised Compilation. Frontiers in Earth Science, 10. https://doi.org/10.3389/feart.2022.907543

Lin, J., & Stein, R. S. (2004). Stress triggering in thrust and subduction earthquakes and stress interaction between the southern San Andreas and nearby thrust and strike-slip faults. Journal of Geophysical Research, 109(B2). https://doi.org/10.1029/2003JB002607

Magee, C., & Jackson, C. A.-L. (2020). Seismic reflection data reveal the 3D structure of the newly discovered Exmouth Dyke Swarm, offshore NW Australia. Solid Earth, 11(2), 579–606. https://doi.org/10.5194/se-11-579-2020

Magee, C., & Jackson, C. A.-L. (2021). Can we relate the surface expression of dike-induced normal faults to subsurface dike geometry? Geology, 49(4), 366–371. https://doi.org/10.1130/G48171.1

Magee, C., Love, V., Fayez, K., Andrews, B., Rivas-Dorado, S., Jackson, C., et al. (2023). Quantifying Dyke-Induced Graben and Dyke Structure Using 3D Seismic Reflection Data and The Role of Interpretation Bias. Τεκτονικα, 1(2), 32–53. https://doi.org/10.55575/tektonika2023.1.2.25

Manighetti, I., King, G., & Sammis, C. G. (2004). The role of off-fault damage in the evolution of normal faults. Earth and Planetary Science Letters, 217. https://doi.org/10.1016/S0012-821X(03)00601-0

Mansfield, C., & Cartwright, J. (2001). Fault growth by linkage: observations and implications from analogue models. Journal of Structural Geology, 23(5), 745–763. https://doi.org/10.1016/S0191-8141(00)00134-6

Mäntyniemi, P., Tatevossian, R. E., & Tatevossian, T. N. (2014). Uncertain historical earthquakes and seismic hazard: theoretical and practical considerations. Geomatics, Natural Hazards and Risk, 5(1), 1–6. https://doi.org/10.1080/19475705.2012.751633

Manzocchi, T., Walsh, J. J., & Nicol, A. (2006). Displacement accumulation from earthquakes on isolated normal faults. Journal of Structural Geology, 28(9), 1685–1693. https://doi.org/10.1016/j.jsg.2006.06.006

Martinez, C., Chiarella, D., Jackson, C. A.-L., Rennie, H., & Scarselli, N. (2024). Syn-rift tectono-stratigraphic development of the Thebe-0 fault system, Exmouth Plateau, offshore NW Australia: The role of fault-scarp degradation. Basin Research, 36(1), e12842. https://doi.org/10.1111/bre.12842

Geoscience Austrailia (2025). National Offshore Petroleum Information Management System (NOPIMS) [Dataset]. https://nopims.dmp.wa.gov.au/nopims

McClymont, A. F., Villamor, P., & Green, A. G. (2009). Fault displacement accumulation and slip rate variability within the Taupo Rift (New Zealand) based on trench and 3-D ground-penetrating radar data. Tectonics, 28(4). https://doi.org/10.1029/2008TC002334

Mechernich, S., Schneiderwind, S., Mason, J., Papanikolaou, I. D., Deligiannakis, G., Pallikarakis, A., et al. (2018). The Seismic History of the Pisia Fault (Eastern Corinth Rift, Greece) From Fault Plane Weathering Features and Cosmogenic 36Cl Dating. Journal of Geophysical Research: Solid Earth, 123(5), 4266–4284. https://doi.org/10.1029/2017JB014600

Meyer, V., Nicol, A., Childs, C., Walsh, J. J., & Watterson, J. (2002). Progressive localisation of strain during the evolution of a normal fault population. Journal of Structural Geology, 24(8), 1215–1231. https://doi.org/10.1016/S0191-8141(01)00104-3

Mia, M. S., Abdelmeguid, M., Harris, R. A., & Elbanna, A. E. (2024). Rupture Jumping and Seismic Complexity in Models of Earthquake Cycles for Fault Stepovers with Off-Fault Plasticity. Bulletin of the Seismological Society of America, 114(3), 1466–1480. https://doi.org/10.1785/0120230249

Mignan, A., Danciu, L., & Giardini, D. (2015). Reassessment of the Maximum Fault Rupture Length of Strike-Slip Earthquakes and Inference on Mmax in the Anatolian Peninsula, Turkey. Seismological Research Letters, 86(3). https://doi.org/10.1785/0220140252

Mildon, Z. K., Roberts, G. P., Faure Walker, J. P., Beck, J., Papanikolaou, I., Michetti, A. M., et al. (2022). Surface faulting earthquake clustering controlled by fault and shear-zone interactions. Nature Communications, 13(1), 7126. https://doi.org/10.1038/s41467-022-34821-5

Milner, K., Page, M. T., Field, E. H., Parsons, T., Biasi, G. P., & Shaw, B. E. (2013). Defining the inversion rupture set via plausibility filters (USGS Open-File Report No. 1165).

Morley, C. K. & Nixon, C. W. (2016). Topological characteristics of simple and complex normal fault networks. Journal of Structural Geology, 84, pp.68-84. https://doi.org/10.1016/j.jsg.2016.01.005

Nicol, A., Watterson, J., Walsh, J. J., & Childs, C. (1996). The shapes, major axis orientations and displacement patterns of fault surfaces. Journal of Structural Geology, 18(2), 235–248. https://doi.org/10.1016/S0191-8141(96)80047-2

Nicol, A., Walsh, J. J., Watterson, J., & Underhill, J. R. (1997). Displacement rates of normal faults. Nature, 390, 157–159. https://doi.org/10.1038/36548

1042 Nicol, A., Walsh, J.J., Berryman, K. Villamor, P. (2006). Interdependence of fault
1043 displacement rates and paleoearthquakes in an active rift. Geology 34, 865 - 868.
1044 https://doi.org/10.1130/G22335.1

1045 Nicol, A., Walsh, J. J., Villamor, P., Seebeck, H., & Berryman, K. R. (2010). Normal fault
1046 interactions, paleoearthquakes and growth in an active rift. Journal of Structural Geology, 32(8),
1047 1101–1113. https://doi.org/10.1016/j.jsg.2010.06.018

1048 Nicol, A, Robinson, R., Van Dissen, R., & Harvison, A. (2016). Variability of recurrence interval
1049 and single-event slip for surface-rupturing earthquakes in New Zealand. New Zealand Journal of
1050 Geology and Geophysics, 59(1), 97–116. https://doi.org/10.1080/00288306.2015.1127822

1051 Nicol, A, Walsh, J., Berryman, K., & Nodder, S. (2005). Growth of a normal fault by the
1052 accumulation of slip over millions of years. Journal of Structural Geology, 27(2), 327–342.
1053 https://doi.org/10.1016/j.jsg.2004.09.002

1054 Nicol, A., Walsh, J., Childs, C. and Manzocchi, T. (2020). The growth of faults. In Understanding
1055 faults (pp. 221-255). Elsevier. https://doi.org/10.1016/B978-0-12-815985-9.00006-0

1056 Nixon, C. W., Bull, J. M., & Sanderson, D. J. (2014). Localized vs distributed deformation
1057 associated with the linkage history of an active normal fault, Whakatane Graben, New Zealand.
1058 Journal of Structural Geology, 69, 266–280. https://doi.org/10.1016/j.jsg.2014.06.005

1059 Nixon, C.W., Sanderson, D.J., Dee, S.J., Bull, J.M., Humphreys, R.J. and Swanson, M.H. (2014).
1060 Fault interactions and reactivation within a normal-fault network at Milne Point, Alaska. AAPG
1061 Bulletin, 98(10), pp.2081-2107. https://doi.org/10.1306/04301413177

1062 Nixon, C. W., McNeill, L. C., Gawthorpe, R. L., Shillington, D. J., Michas, G., Bell, R. E., et al.
1063 (2024). Increasing fault slip rates within the Corinth Rift, Greece: A rapidly localising active rift
1064 fault network. Earth and Planetary Science Letters, 636, 118716.
1065 https://doi.org/10.1016/j.epsl.2024.118716

1066 Mouslopoulou, V., Walsh, J.J. and Nicol, A. (2009). Fault displacement rates on a range of
1067 timescales. Earth and Planetary Science Letters, 278(3-4), 186-197.
1068 https://doi.org/10.1016/j.epsl.2008.11.031

1069 Onderdonk, N. W., McGill, S. F., & Rockwell, T. K. (2015). Short-term variations in slip rate and
1070 size of prehistoric earthquakes during the past 2000 years on the northern San Jacinto fault
1071 zone, a major plate-boundary structure in southern California. Lithosphere, 7(3), 211–234.
1072 https://doi.org/10.1130/L393.1

1073 Pace, B., Bocchini, G. M., & Boncio, P. (2014). Do static stress changes of a moderate-magnitude
1074 earthquake significantly modify the regional seismic hazard? Hints from the L'Aquila 2009
1075 normal-faulting earthquake (Mw 6.3, central Italy). Terra Nova, 26(6), 430–439.
1076 https://doi.org/10.1111/ter.12117

1077 Pace, B., Visini, F., & Peruzza, L. (2016). FiSH : MATLAB Tools to Turn Fault Data into Seismic-
1078 Hazard Models. Seismological Research Letters, 87(JANUARY), 1–13.
1079 https://doi.org/10.1785/0220150189

1080 Pan, S., Bell, R. E., Jackson, C. A.-L., & Naliboff, J. (2022). Evolution of normal fault displacement
1081 and length as continental lithosphere stretches. Basin Research, 34(1), 121–140.
1082 https://doi.org/10.1111/bre.12613

1083 Peacock, D. C. P., Nixon, C. W., Rotevatn, A., Sanderson, D. J., & Zuluaga, L. F. (2017). Interacting
1084 faults. Journal of Structural Geology, 97, 1–22. https://doi.org/10.1016/j.jsg.2017.02.008

1085 Pesci, A., Teza, G., & Casula, G. (2009). Improving strain rate estimation from velocity data of
1086 non-permanent GPS stations: the Central Apennine study case (Italy). GPS Solutions, 13(4),
1087 249–261. https://doi.org/10.1007/s10291-009-0118-3

1088 Reeve, M. T., Jackson, C. A.-L., Bell, R. E., Magee, C., & Bastow, I. D. (2016). The stratigraphic
1089 record of prebreakup geodynamics: Evidence from the Barrow Delta, offshore Northwest
1090 Australia. Tectonics, 35(8), 1935–1968. https://doi.org/10.1002/2016TC004172

1091 Reeve, M. T., Magee, C., Jackson, C. a.-L., Bell, R., & Bastow, I. D. (2022). Stratigraphic record of
1092 continental breakup, offshore NW Australia. Basin Research, 34(3), 1220–1243.
1093 https://doi.org/10.1111/bre.12656

1094 Roberts, G. P. (2007). Fault orientation variations along the strike of active normal fault systems
1095 in Italy and Greece: Implications for predicting the orientations of subseismic-resolution faults
1096 in hydrocarbon reservoirs. AAPG Bulletin, 91(1), 1–20. https://doi.org/10.1306/08300605146

1097 Roberts, G. P., Sgambato, C., Mildon, Z. K., Iezzi, F., Beck, J., Robertson, J., et al. (2024). Spatial
1098 migration of temporal earthquake clusters driven by the transfer of differential stress between
1099 neighbouring fault/shear-zone structures. Journal of Structural Geology, 181, 105096.
1100 https://doi.org/10.1016/j.jsg.2024.105096

1101 Roberts, G. P., Iezzi, F., Sgambato, C., Robertson, J., Beck, J., Mildon, Z. K., et al. (2025).
1102 Characteristics and modelling of slip-rate variability and temporal earthquake clustering across
1103 a distributed network of active normal faults constrained by in situ 36Cl cosmogenic dating of

1104 fault scarp exhumation, central Italy. Journal of Structural Geology, 195, 105391.
1105 https://doi.org/10.1016/j.jsg.2025.105391

1106 Roberts, Gerald P, & Michetti, A. M. (2004). Spatial and temporal variations in growth rates
1107 along active normal fault systems: an example from The Lazio–Abruzzo Apennines, central Italy.
1108 Journal of Structural Geology, 26(2), 339–376. https://doi.org/10.1016/S0191-8141(03)00103-2

1109 Roche, V., Homberg, C., & Rocher, M. (2013). Fault nucleation, restriction, and aspect ratio in
1110 layered sections: Quantification of the strength and stiffness roles using numerical modeling.
1111 Journal of Geophysical Research: Solid Earth, 118(8), 4446–4460.
1112 https://doi.org/10.1002/jgrb.50279

1113 Rodriguez Piceda, C., Mildon, Z. K., van den Ende, M., Ampuero, J.P., & Andrews, B. J. (2025).
1114 Normal Fault Interactions in Seismic Cycles and the Impact of Fault Network Geometry. Journal
1115 of Geophysical Research: Solid Earth, 130(4), e2024JB030382.
1116 https://doi.org/10.1029/2024JB030382

1117 Romanet, P., Bhat, H. S., Jolivet, R., & Madariaga, R. (2018). Fast and Slow Slip Events Emerge
1118 Due to Fault Geometrical Complexity. Geophysical Research Letters, 45(10), 4809–4819.
1119 https://doi.org/10.1029/2018GL077579

1120 Rotevatn, A., Jackson, C. A. L., Tvedt, A. B. M., Bell, R. E., & Blækkan, I. (2019). How do normal
1121 faults grow? Journal of Structural Geology, (August), 0–1.
1122 https://doi.org/10.1016/j.jsg.2018.08.005

1123 Schaaf, A., & Bond, C. E. (2019). Quantification of uncertainty in 3-D seismic interpretation:
1124 implications for deterministic and stochastic geomodeling and machine learning. Solid Earth,
1125 10(4), 1049–1061. https://doi.org/10.5194/se-10-1049-2019

1126 Schlagenhauf, A., Manighetti, I., Malavieille, J., & Dominguez, S. (2008). Incremental growth of
1127 normal faults: Insights from a laser-equipped analog experiment. Earth and Planetary Science
1128 Letters, 273(3), 299–311. https://doi.org/10.1016/j.epsl.2008.06.042

1129 Scholz, C. H., & Contreras, J. C. (1998). Mechanics of continental rift architecture. Geology,
1130 26(11), 967–970. https://doi.org/10.1130/0091-7613(1998)026<0967:MOCRA>2.3.CO;2

1131 Schwartz, D. P., & Coppersmith, K. J. (1984). Fault behavior and characteristic earthquakes:
1132 examples from the Wasatch and San Andreas fault zones (USA). J. Geophys. Res., 89(B7), 5681–
1133 5698. https://doi.org/10.1029/JB089iB07p05681

1134 Scotti, O., Visini, F., Faure Walker, J., Peruzza, L., Pace, B., Benedetti, L., et al. (2021). Which
1135 Fault Threatens Me Most? Bridging the Gap Between Geologic Data-Providers and Seismic Risk
1136 Practitioners. Frontiers in Earth Science, 8. https://doi.org/10.3389/feart.2020.626401

1137 Sgambato, C., Faure Walker, J. P., & Roberts, G. P. (2020). Uncertainty in strain-rate from field
1138 measurements of the geometry, rates and kinematics of active normal faults: Implications for
1139 seismic hazard assessment. Journal of Structural Geology, 131, 103934.
1140 https://doi.org/10.1016/j.jsg.2019.103934

1141 Sgambato, C., Faure Walker, J. P., Roberts, G. P., Mildon, Z. K., & Meschis, M. (2023). Influence
1142 of Fault System Geometry and Slip Rates on the Relative Role of Coseismic and Interseismic
1143 Stresses on Earthquake Triggering and Recurrence Variability. Journal of Geophysical Research:
1144 Solid Earth, 128(11), e2023JB026496. https://doi.org/10.1029/2023JB026496

1145 Sgambato, C., Roberts, G. P., Iezzi, F., Faure Walker, J. P., Beck, J., Mildon, Z. K., et al. (2025).
1146 Millennial Slip-Rates Variability of Along-Strike Active Faults in the Italian Southern Apennines
1147 Revealed by Cosmogenic 36Cl Dating of Fault Scarps. Tectonics, 44(3), e2024TC008529.
1148 https://doi.org/10.1029/2024TC008529

1149 Shaw, B. E., Milner, K., Field, E. H., Richards-Dinger, K., Gilchrist, J. J., Dieterich, J. H., & Jordan,
1150 T. H. (2018). A physics-based earthquake simulator replicates seismic hazard statistics across
1151 California. Science Advances, 4(8). https://doi.org/10.1126/sciadv.aau0688

1152 Soliva, R., Benedicto, A., & Maerten, L. (2006). Spacing and linkage of confined normal faults:
1153 Importance of mechanical thickness. Journal of Geophysical Research: Solid Earth, 111(1), 1–17.
1154 https://doi.org/10.1029/2004JB003507

1155 Stein, R. S. (1999). The role of stress transfer in earthquake occurrence. Nature, 402(6762),
1156 605–609. https://doi.org/10.1038/45144

1157 Swafford, L., & Stein, S. (2007). Limitations of the short earthquake record for seismicity and
1158 seismic hazard studies. In S. Stein & S. Mazzotti (Eds.), Continental Intraplate Earthquakes:
1159 Science, Hazard, and Policy Issues (p. 0). Geological Society of America.
1160 https://doi.org/10.1130/2007.2425(04)

1161 Sylvester, A. G. (1988). Strike-slip faults. GSA Bulletin, 100(11), 1666–1703.
1162 https://doi.org/10.1130/0016-7606(1988)100%253C1666:SSF%253E2.3.CO;2

1163 Taylor, S. K., Nicol, A., & Walsh, J. J. (2008). Displacement loss on growth faults due to sediment
1164 compaction. Journal of Structural Geology, 30(3), 394–405.
1165 https://doi.org/10.1016/j.jsg.2007.11.006

1166 Toda, S., & Enescu, B. (2011). Rate/state Coulomb stress transfer model for the CSEP Japan
1167 seismicity forecast. Earth, Planets and Space, 63(3), 171–185.
1168 https://doi.org/10.5047/eps.2011.01.004

1169 Toda, S., & Stein, R. S. (2018). Why Aftershock Duration Matters for Probabilistic Seismic Hazard
1170 Assessment. Bull. Seismol. Soc. Am., 108(3), 1414–1426. https://doi.org/10.1785/0120170270

1171 Toda, S., Stein, R. S., Reasenberg, P. A., Dieterich, J. H., & Yoshida, A. (1998). Stress transferred
1172 by the 1995 Mw = 6.9 Kobe, Japan, shock: Effect on aftershocks and future earthquake
1173 probabilities. Journal of Geophysical Research: Solid Earth, 103(B10), 24543–24565.
1174 https://doi.org/10.1029/98JB00765

1175 Torabi, A., & Berg, S. S. (2011). Scaling of fault attributes: A review. Marine and Petroleum
1176 Geology, 28(8), 1444–1460. https://doi.org/10.1016/j.marpetgeo.2011.04.003

1177 Valentini, A., Visini, F., & Pace, B. (2017). Integrating faults and past earthquakes into a
1178 probabilistic seismic hazard model for peninsular Italy. Natural Hazards and Earth System
1179 Sciences, 17(11), 2017–2039. https://doi.org/10.5194/nhess-17-2017-2017

1180 Verdecchia, A., Carena, S., Pace, B., & DuRoss, C. B. (2019). The effect of stress changes on time-
1181 dependent earthquake probabilities for the central Wasatch fault zone, Utah, USA. Geophysical
1182 Journal International, 219(2), 1065–1081. https://doi.org/10.1093/gji/ggz336

1183 Walsh, J. J., Childs, C., Imber, J., Manzocchi, T., Watterson, J., & Nell, P. A. R. (2003). Strain
1184 localisation and population changes during fault system growth within the Inner Moray Firth,
1185 Northern North Sea. Journal of Structural Geology, 25(2), 307–315.
1186 https://doi.org/10.1016/S0191-8141(02)00028-7

1187 Walsh, J.J., Nicol, A. and Childs, C. (2002). An alternative model for the growth of faults. Journal
1188 of Structural Geology, 24(11), 1669-1675. https://doi.org/10.1016/S0191-8141(01)00165-1

1189 Wechsler, N., Rockwell, T. K., & Klinger, Y. (2018). Variable slip-rate and slip-per-event on a
1190 plate boundary fault: The Dead Sea fault in northern Israel. Tectonophysics, 722, 210–226.
1191 https://doi.org/10.1016/j.tecto.2017.10.017

1192 Weldon, R., Scharer, K., Fumal, T., & Biasi, G. (2004). Wrightwood and the earthquake cycle:
1193 What a long recurrence record tells us about how faults work. GSA Today, 14(9), 4–10.
1194 https://doi.org/10.1130/1052-5173(2004)014%253C4:WATECW%253E2.0.CO;2

1195 Williams, J. N., Werner, M. J., Goda, K., Wedmore, L. N., De Risi, R., Biggs, J., et al. (2023). Fault-
1196 based probabilistic seismic hazard analysis in regions with low strain rates and a thick

seismogenic layer: a case study from Malawi. Geophysical Journal International, 233(3), 2172–2207. https://doi.org/10.1093/gji/ggad060

Woodcock, N. (1986). The role of strike-slip fault systems at plate boundaries. Philosophical Transactions of the Royal Society of London. Series A, Mathematical and Physical Sciences, 317(1539). https://royalsocietypublishing.org/doi/abs/10.1098/rsta.1986.0021

Yin, Y., Galvez, P., Heimisson, E. R., & Wiemer, S. (2023). The role of three-dimensional fault interactions in creating complex seismic sequences. Earth and Planetary Science Letters, 606, 118056. https://doi.org/10.1016/j.epsl.2023.118056

Youngs, R. R., & Coppersmith, K. J. (1985). Implications of fault slip rates and earthquake recurrence models to probabilistic seismic hazard estimates. Bulletin of the Seismological Society of America, 75(4), 939–964. https://doi.org/10.1785/BSSA0750040939

Zinke, R., Dolan, J. F., Rhodes, E. J., Van Dissen, R., McGuire, C. P., Hatem, A. E., et al. (2019). Multimillennial Incremental Slip Rate Variability of the Clarence Fault at the Tophouse Road Site, Marlborough Fault System, New Zealand. Geophysical Research Letters, 46(2), 717–725. https://doi.org/10.1029/2018GL080688

Figure captions

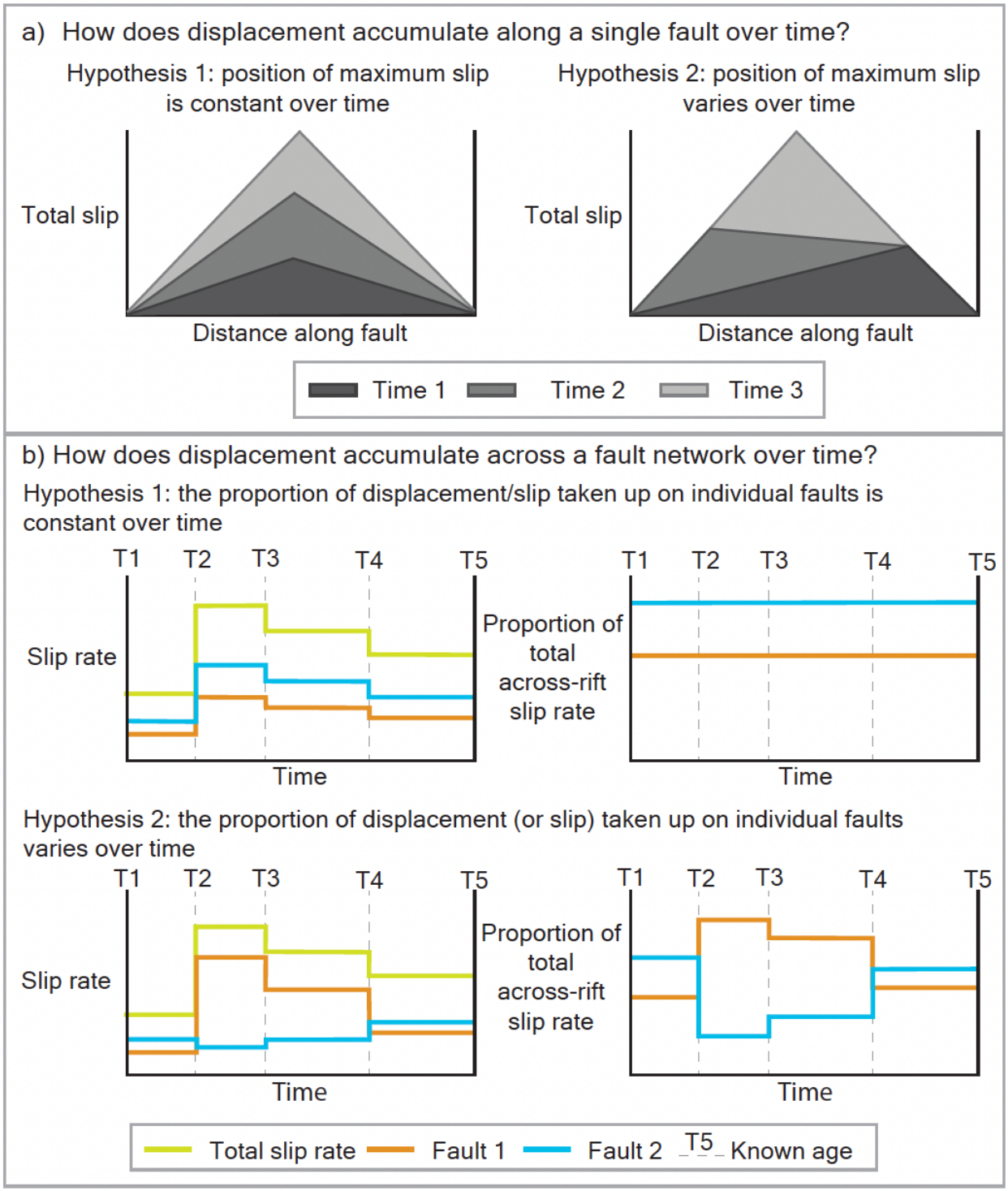

Figure 1 – Two questions and examples of associated hypotheses that will be tested in this study.

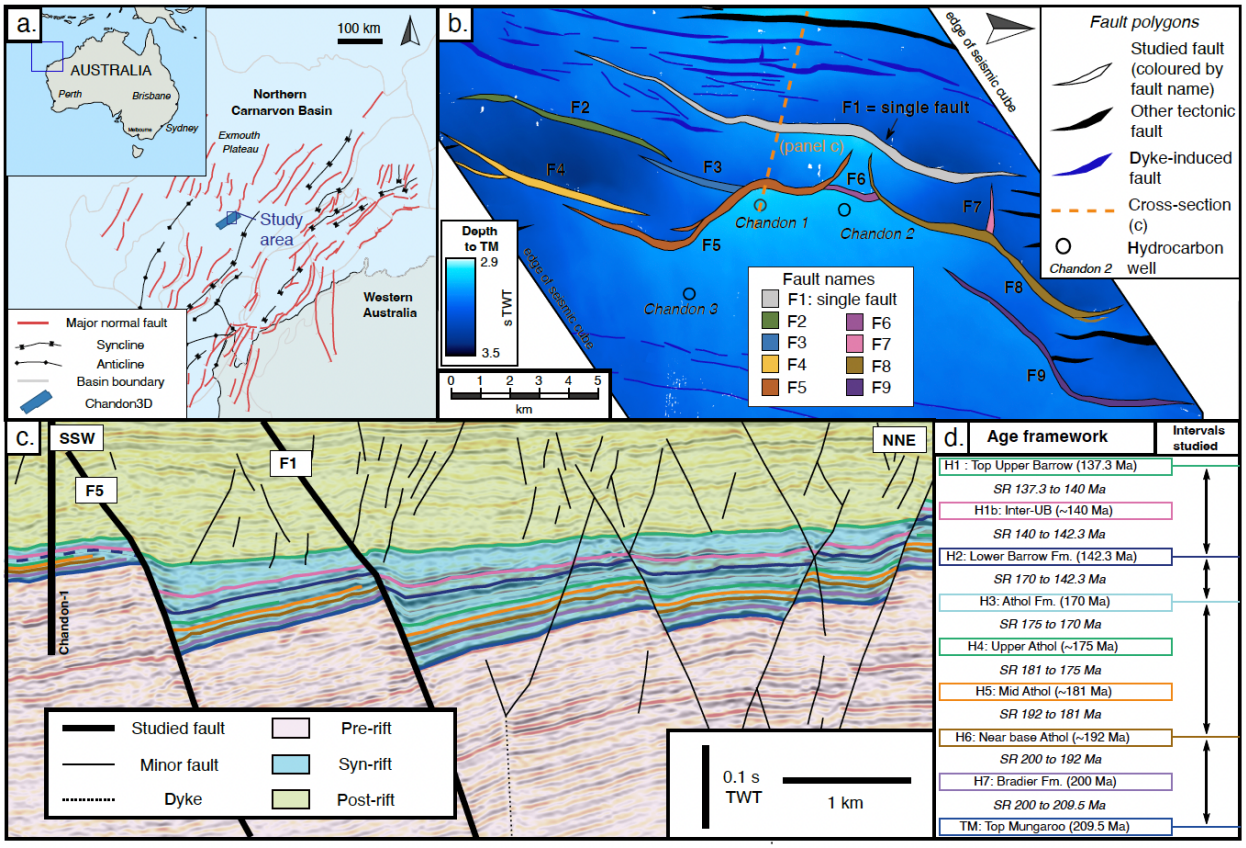

Figure 2 – Overview of the Chandon 3D seismic cube used in this study. a) Location of the Chandon 3D seismic cube. b) Depth to base syn-rift horizon (Top Mungaroo, TM) showing the locations of faults and the distribution of throw across the area. Open circles show the locations of wells used to provide age constraints on the stratigraphy of the area. The single fault with relatively simple geometry that is first studied is indicated. The studied fault network is shown as black fault polygons. c) Seismic cross-section across the fault network of interest, showing the key horizons and ages used in this study. d) Stratigraphic age framework used to determine the slip rates over different time periods, where the ages are given with a ~, these are approximate ages based on constant sedimentation rates, and where ~ is not present, the ages

refer to local ages derived from well reports (see main text for further discussion on age related uncertainties).

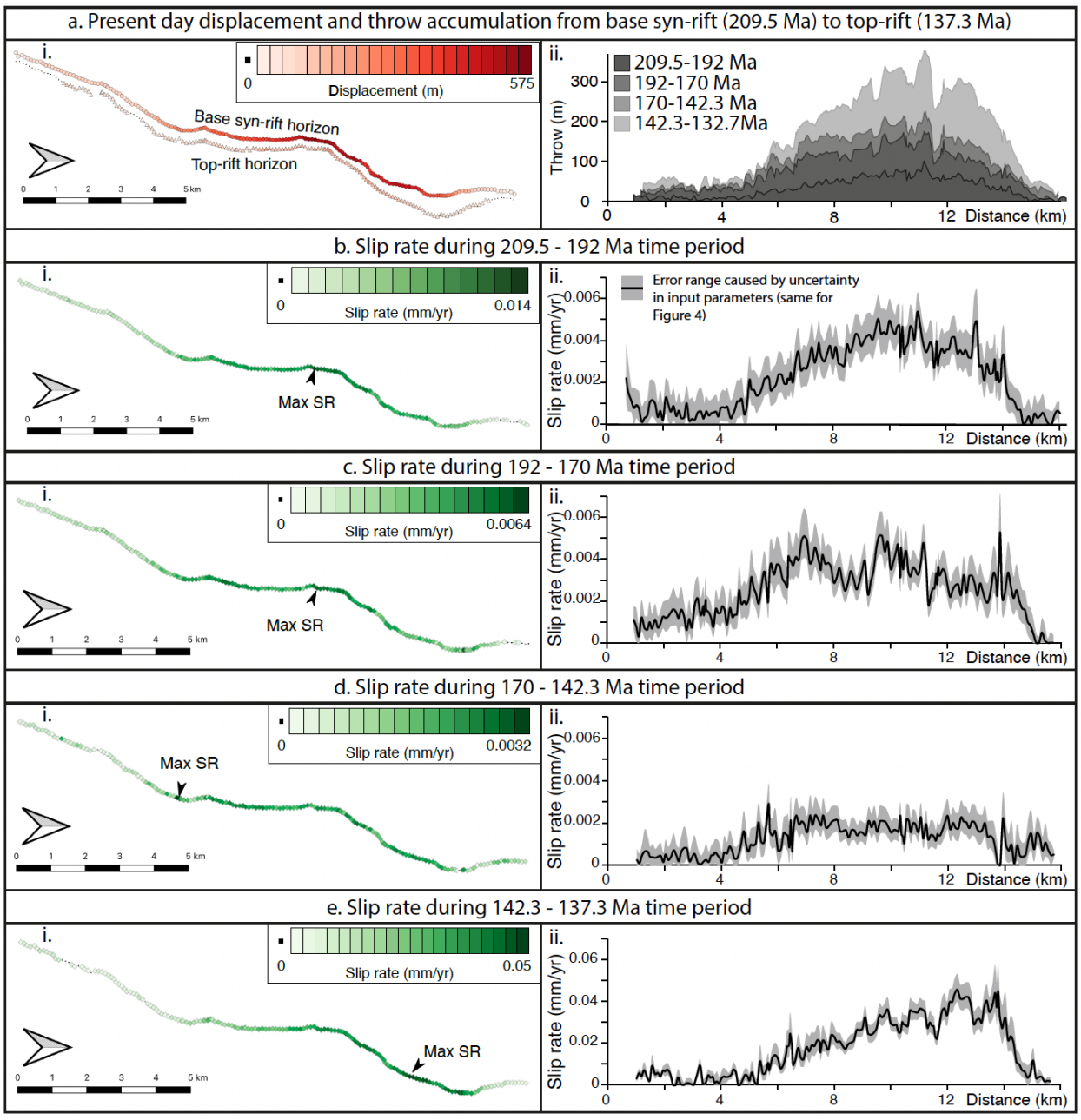

Figure 3 – Variation of slip rate through time along a single fault with relatively simple geometry. a. i. Present day geometry and throw at the base syn-rift (TM, Top Mungaroo) and the top rift horizon (H1, Top Upper Barrow). ii. The cumulative throw plotted for the four studied time intervals between 209.5 and 137.3 Ma and plotted against distance along the fault trace. b-e. Slip rates during different time periods, plotted as i) a colour scale along the fault trace in map view and ii) against distance along the fault (with errors relating to the minimum

and maximum slip-rate calculated shown by the grey box). Note that the colour scale and vertical axis change scale in each of these sub-plots. Both the magnitude of slip rate and the shape of the slip rate profile changes throughout time.

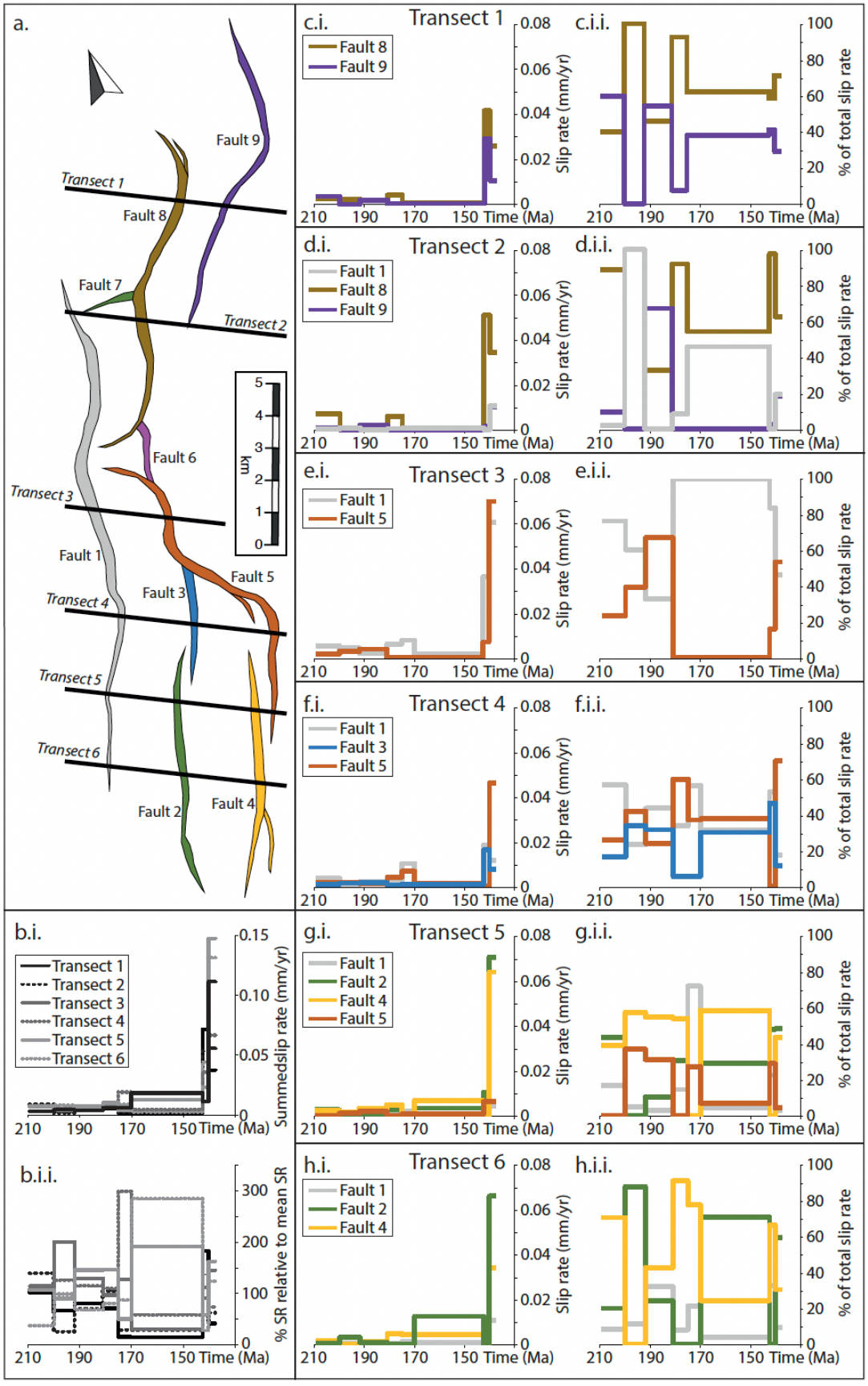
a.
Fault 9
Transect 1
Fault 8
Fault 7
Transect 2
Fault 6
Transect 3
Fault 1
Fault 3
Fault 5
Transect 4
Transect 5
Transect 6
Fault 2
Fault 4
km
0
1
2
3
4
5
c.i.
Transect 1
Fault 8
Fault 9
c.i.i.
d.i.
Transect 2
Fault 1
Fault 8
Fault 9
d.i.i.
e.i.
Transect 3
Fault 1
Fault 5
e.i.i.
f.i.
Transect 4
Fault 1
Fault 3
Fault 5
f.i.i.
g.i.
Transect 5
Fault 1
Fault 2
Fault 4
Fault 5
g.i.i.
h.i.
Transect 6
Fault 1
Fault 2
Fault 4
h.i.i.
Slip rate (mm/yr)
0
0.02
0.04
0.06
0.08
% of total slip rate
0
20
40
60
80
100
210
190
170
150
Time (Ma)
b.i.
Transect 1
Transect 2
Transect 3
Transect 4
Transect 5
Transect 6
Summedslip rate (mm/yr)
0
0.05
0.10
0.15
b.i.i.
% SR relative to mean SR
0
100
200
300

1238

Figure 4 – Along-strike variations in slip rate across the fault network. a) Present day throw across the i) base syn rift horizon (TM) and ii) cumulative throw plots for individual faults and the fault network. Each shade in the cumulative throw plots represents the throw accumulated in a specific time period, the solid colour represents the throw accumulated in the earliest time period, the lighter colours are for later time periods, and the colours match those used in Figure 5. b-e) Slip-rate shown in both map view and as profiles for the four studied time periods. To enable overall profile trends to be explored, the data was smoothed using a window sample of 10 datapoints, for raw data please see Supplementary 3. Note that Fault 4 is two separate faults (4a and 4b) in the first time period (b), and they coalesce together in later time periods.

Also, the colour scales of panels i and vertical scales in panels ii differ to better show the trends within a given time period.

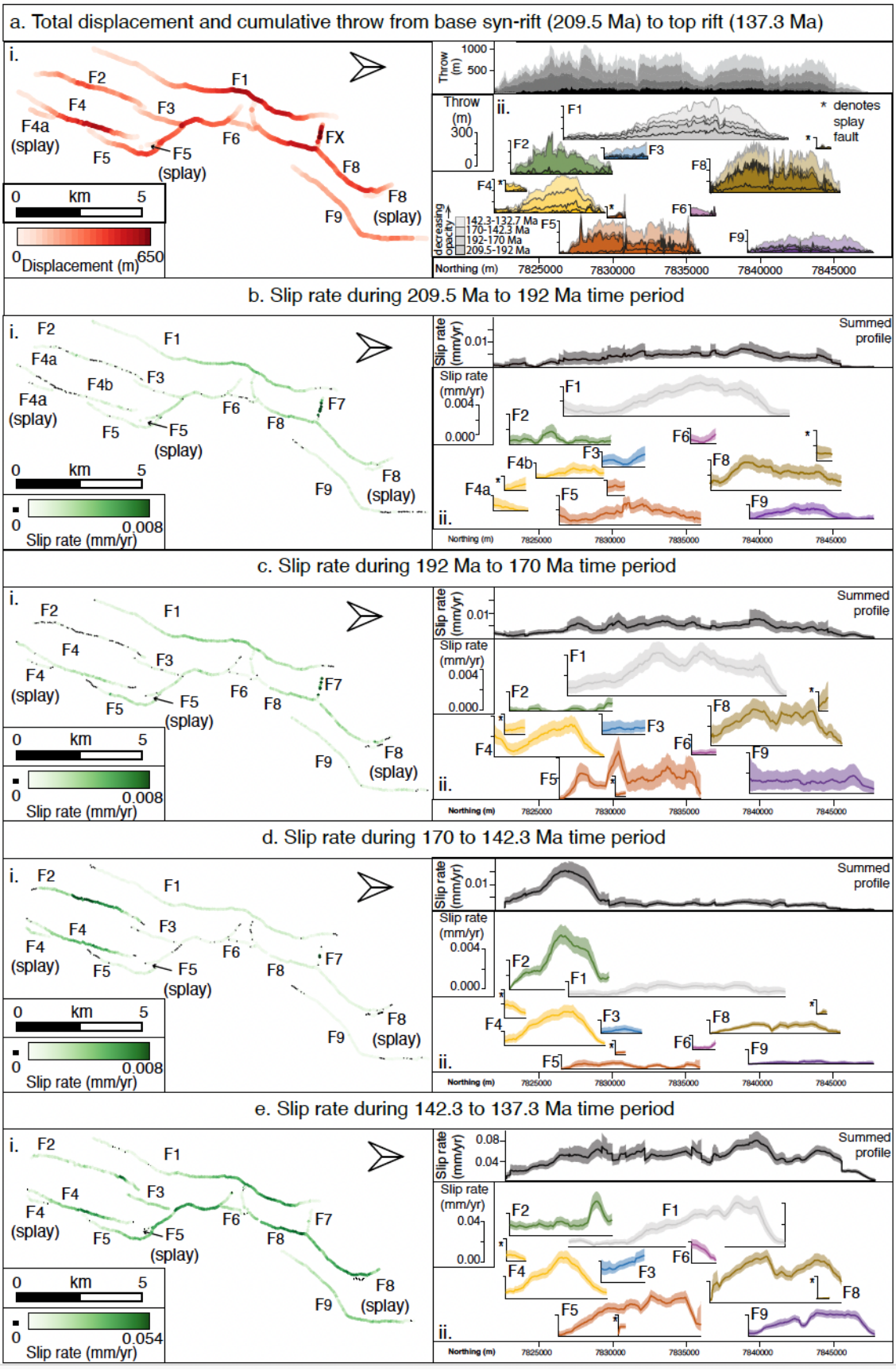
a. Total displacement and cumulative throw from base syn-rift (209.5 Ma) to top rift (137.3 Ma)
i.
F1
F2
F3
F4
F4a
(splay)
F5
F5
(splay)
F6
FX
F8
F8
(splay)
F9
0 km 5
0 Displacement (m) 650
Throw (m)
1000
500
Throw (m)
300
0
ii.
* denotes splay fault
decreasing opacity
142.3-132.7 Ma
170-142.3 Ma
192-170 Ma
209.5-192 Ma
Northing (m)
7825000
7830000
7835000
7840000
7845000
b. Slip rate during 209.5 Ma to 192 Ma time period
F4b
F7
0 km 5
0 0.008 Slip rate (mm/yr)
Slip rate (mm/yr)
0.01
Summed profile
0.004
0.000
c. Slip rate during 192 Ma to 170 Ma time period
d. Slip rate during 170 to 142.3 Ma time period
e. Slip rate during 142.3 to 137.3 Ma time period
0 0.054 Slip rate (mm/yr)
0.08
0.04
0.04
0.00

1250

1251 Figure 5 – Slip rate variations across a fault network. a) Fault polygons for the base syn-rift
1252 horizon showing the locations of the transects taken perpendicular to the overall strike of the
1253 fault network. The colour coding of each fault is consistent throughout the figure. b) Cumulative
1254 slip rate along each transect (i), calculated by summing the individual slip rates for each fault.
1255 This shows the general pattern of the fault network speeding up and slowing down over time.
1256 The balance of slip rate along-strike of the fault network is shown to vary over time (ii). c-h) Slip
1257 rate changes for faults along each individual transect, shown as absolute slip rate values (i) and
1258 as a percentage of the total slip rate along each transect (ii). Note that the percentage of slip-

rate taken up on individual faults varies with time, indicating that the relative dominance of faults in this small rift is changing over time.

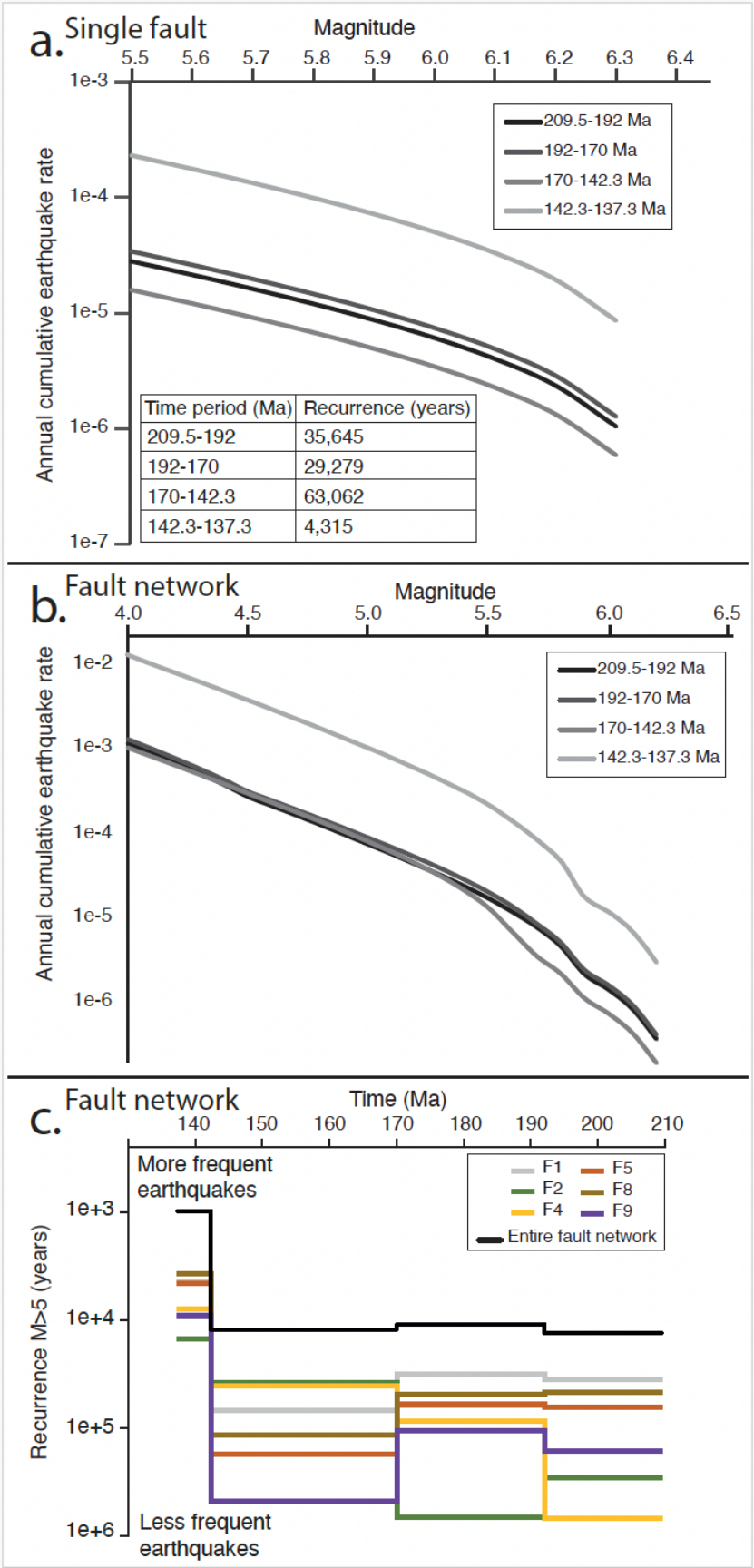
a. Single fault
Magnitude
5.5 5.6 5.7 5.8 5.9 6.0 6.1 6.2 6.3 6.4
1e-3
1e-4
1e-5
1e-6
1e-7
Annual cumulative earthquake rate
209.5-192 Ma
192-170 Ma
170-142.3 Ma
142.3-137.3 Ma
Time period (Ma) | Recurrence (years)
209.5-192 | 35,645
192-170 | 29,279
170-142.3 | 63,062
142.3-137.3 | 4,315
b. Fault network
Magnitude
4.0 4.5 5.0 5.5 6.0 6.5
1e-2
1e-3
1e-4
1e-5
1e-6
Annual cumulative earthquake rate
209.5-192 Ma
192-170 Ma
170-142.3 Ma
142.3-137.3 Ma
c. Fault network
Time (Ma)
140 150 160 170 180 190 200 210
More frequent earthquakes
1e+3
1e+4
1e+5
1e+6
Less frequent earthquakes
Recurrence M>5 (years)
F1 F5
F2 F8
F4 F9
Entire fault network

Figure 6 – Earthquake rate calculations utilising variable slip rates. a. Annual cumulative rate of earthquakes for the single fault, using the slip rates derived from different time intervals. The variation in recurrence interval for earthquakes M>5.5 is tabulated. This shows that the order of magnitude variation in slip rate results in an order of magnitude variation in the recurrence interval. b. Annual cumulative rate of earthquakes for the fault network studied, using the slip rates derived from different time intervals. The time interval with the highest slip rate (Figure 4a) has the highest annual cumulative earthquake rate. c. Variation over time in recurrence interval for M>5 earthquakes on individual faults and for the whole fault network. Similar to the proportion of slip rate (Figure 4d), the fault with the highest hazard (i.e. the smallest recurrence interval) varies throughout time. The total hazard across the system also varies with time, similar to the total slip rate across the network (Figure 2b).

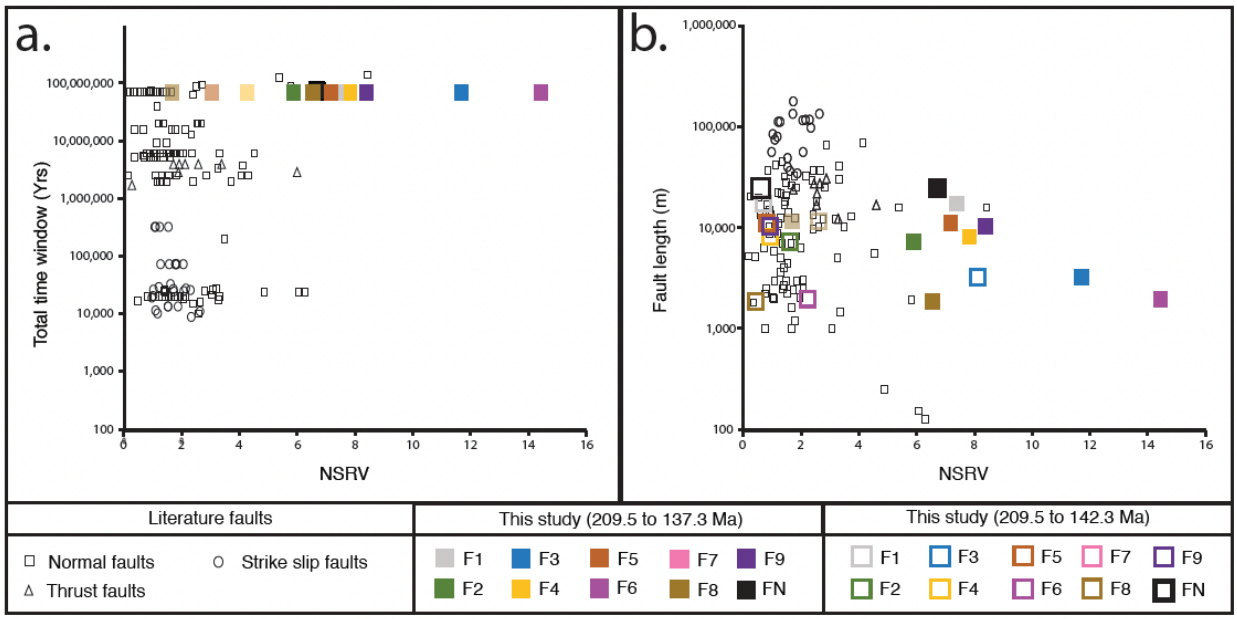

Figure 7: Normalised slip-rate variability (NSRV) calculated for the studied faults and a compilation of normal (n = 108), strike-slip (n = 27) and thrust (n = 8) faults that show incremental variations in slip-rate across their growth histories. For the full dataset, and source publications, please see Supplementary 6. NSRV is plotted against the a) total time period that slip-rate is investigated over and b) fault length. Data from this study is colour coded by fault, faults splay data are shown in the same colour with transparency applied. When the last time period (142.3-137.3Ma) is omitted from calculating the NSRV, all values are lower (Table S6.3) and are plotted on b) for comparison.